Fatigue testing and analysis of steel plates manufactured by wire-arc directed energy deposition

HUANG, Cheng, LI, Lingzhen <http://orcid.org/0000-0001-8887-4498>, PICHLER, Niels <http://orcid.org/0000-0002-8602-3291>, GHAFOORI, Elyas <http://orcid.org/0000-0002-4924-0668>, SUSMEL, Luca <http://orcid.org/0000-0001-7753-9176> and GARDNER, Leroy <http://orcid.org/0000-0003-0126-6807>

Additive Manufacturing 73 (2023) 103696

Contents lists available at ScienceDirect

Additive Manufacturing

journal homepage: www.elsevier.com/locate/addma

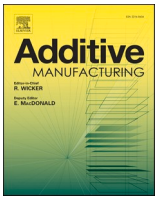

Fatigue testing and analysis of steel plates manufactured by wire-arc directed energy deposition

Cheng Huang [a], Lingzhen Li [b,c,*], Niels Pichler [b,c], Elyas Ghafoori [b,c,d], Luca Susmel [e], Leroy Gardner [a]

[a] Department of Civil and Environmental Engineering, Imperial College London, UK
[b] Empa, Swiss Federal Laboratories for Materials Science and Technology, Switzerland
[c] Department of Civil, Environmental and Geomatic Engineering, ETH Zürich, Switzerland
[d] Institute for Steel Construction, Faculty of Civil Engineering and Geodetic Science, Leibniz University Hannover, Germany
[e] Department of Civil and Structural Engineering, The University of Sheffield, UK

ARTICLE INFO

Keywords:
Directed energy deposition (DED)
Experiments
Fatigue life
Geometric variability
Metal 3D printing
Stress concentrations

ABSTRACT

Wire-arc directed energy deposition (DED), also known as wire-arc additive manufacturing (WAAM), is a metal 3D printing technique that is recognised for its high efficiency, cost-effectiveness, flexibility in build scales and suitability for the construction sector. However, there remains a lack of fundamental data on the structural performance of WAAM elements, especially regarding their fatigue behaviour. A comprehensive experimental study into the fatigue behaviour of WAAM steel plates has therefore been undertaken and is reported herein. Following geometric, mechanical and microstructural characterisation, a series of WAAM coupons was tested under uniaxial high-cycle fatigue loading. A total of 75 fatigue tests on both as-built and machined coupons, covering various stress ranges and stress ratios ($R = 0.1$, 0.2, 0.3 and 0.4), have been conducted. The local stress concentrations in the as-built coupons induced by their surface undulations have also been studied by numerical simulations. The fatigue test results were analysed using constant life diagrams (CLDs) and *S-N* (stress-life) diagrams, based on both nominal and local stresses. The CLDs revealed that the fatigue strength of the as-built WAAM steel was relatively insensitive to the different stress ratios. The *S-N* diagrams showed that the surface undulations resulted in a reduction of about 35% in the fatigue endurance limit for the as-built WAAM material relative to the machined material, and a reduction of about 60% in fatigue life under the same load level. The as-built and machined WAAM coupons were shown to exhibit similar fatigue behaviour to conventional steel butt welds and S355 structural steel plates, respectively. Preliminary nominal stress-based and local stress-based *S-N* curves were also proposed for the WAAM steel.

1. Introduction

The recent emergence of metal 3D printing within the construction industry has generated great interest from architects and structural engineers [1–8]. Wire-arc directed energy deposition (DED), also termed wire-arc additive manufacturing (WAAM), is a method of metal 3D printing that employs conventional welding technology and advanced robotics to build parts in a layer-by-layer fashion. Distinguished from the other metal 3D printing methods [9], WAAM enables large-scale parts to be built with reasonable manufacturing times and costs, and is thus deemed well-suited to structural engineering applications. Early structural uses of WAAM have featured the MX3D footbridge in Amsterdam [10], a steel footbridge in Darmstadt [11] and intricate connection nodes [12].

With the growing interest in the use of WAAM in construction, it is essential to develop a clear understanding of the material and structural behaviour of WAAM elements. The MX3D bridge project [10] launched a comprehensive series of experimental verification studies on WAAM elements, investigating their performance at the material [13,14], cross-section [14–16], member [17] and structural [10] levels, with an emphasis on structural stability. It has been found that WAAM stainless steels typically exhibit a strong degree of anisotropy [13], while WAAM carbon steels generally display almost isotropic mechanical properties [2,18]. The geometric variability inherent to the WAAM process has

* Corresponding author at: Empa, Swiss Federal Laboratories for Materials Science and Technology, Switzerland.
E-mail address: lingzhen.li@empa.ch (L. Li).

https://doi.org/10.1016/j.addma.2023.103696
Received 8 March 2023; Received in revised form 30 June 2023; Accepted 13 July 2023
Available online 17 July 2023

been shown to result in a weakening in the mechanical and structural behaviour of WAAM elements [13,15–19]. This weakening effect is deemed to be more significant for WAAM elements under fatigue loading than under static loading, due to the increased susceptibility to local stress concentrations caused by geometric discontinuities.

Fatigue fracture accounts for about 80% of all structural failures [20,21] and has long been an issue of concern in civil engineering [22–28]. Studies into the fatigue properties of WAAM materials have only emerged in recent years and have largely focused on stainless steels [29–34], titanium alloys [35–38] and other alloys [39–42]. More recently, WAAM carbon steels have become the subject of increasing attention. Bartsch et al. [43] conducted a series of fatigue tests and extensive finite element simulations on as-built WAAM steel parts to examine their fatigue resistance. Dirisu et al. [44] investigated means of mitigating the influence of the surface undulations of as-built WAAM plates by post-rolling, which relieved the stress concentration effects and hence led to improved fatigue performance. Ermakova et al. [45,46] and Huang et al. [47] performed fatigue crack growth (FCG) tests on machined WAAM normal- and high-strength steel specimens, revealing similar FCG behaviour to that of equivalent, conventionally produced steels, with no significant anisotropy observed [47]. In addition to high-cycle fatigue, the low-cycle fatigue behaviour and failure mechanisms of WAAM steels have also been studied [48].

Thus far, the fatigue behaviour of WAAM steels has yet to be fully characterised. To bridge this knowledge gap, a comprehensive series of high-cycle fatigue tests on WAAM steel plates has been conducted and is presented herein. The production, geometric measurement and mechanical and microstructural testing of the WAAM material are first described. Fatigue testing of a series of as-built and machined WAAM coupons is then presented, followed by numerical analyses of the local stress concentrations in the as-built coupons. Finally, the fatigue behaviour of the examined WAAM steel plates is assessed using constant life diagrams (CLDs) and *S-N* (stress range versus number of cycles to failure) diagrams, and compared against that of conventional steel butt welds and S355 structural steel.

2. Experimental programme

2.1. Test specimens

Flat plates of 3 mm nominal thickness were cut from oval tubes (with flat sides) – see Fig. 1, printed by MX3D [49] using their proprietary multi-axis robotic WAAM technology. The feedstock material was ER70S-6 (EN ISO 14341-A G 42 3M21 3Si1) steel wire (with a diameter of 0.8 mm), the chemical composition and mechanical properties of which have been reported in [18]. The WAAM plates were manufactured using a parallel deposition strategy [2,18] on a 300 × 300 × 20 mm^3 S235 steel base plate, with the deposition direction reversed every three layers – see Fig. 2 (a). A summary of the key WAAM process parameters, as provided by the manufacturer, is given in Table 1. The printing parameters were also adopted in previous research [18,47] and were kept constant during the WAAM process; this would lead to increasing interpass temperatures with the deposition of layers and hence varying material properties [50]. The variation in material properties has however been found to feature mainly within the bottom region of WAAM steel plates [18], and is not deemed to affect the results of the material tests performed herein since the test specimens were extracted away from the base plate where the interpass temperature would have been essentially constant.

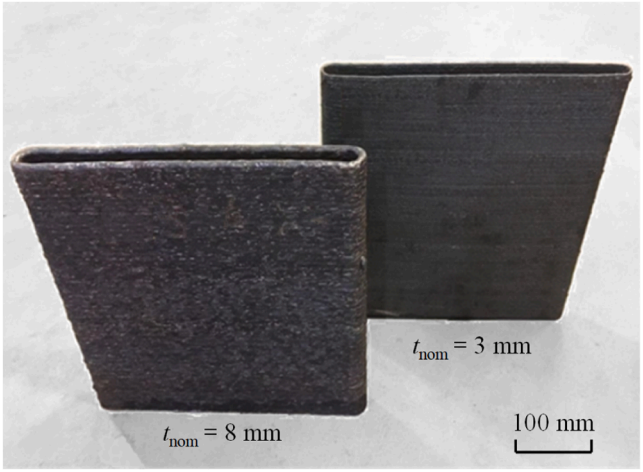

Fig. 1. WAAM oval tubes of 3 mm (and 8 mm) nominal thickness [18,47].

Static and fatigue coupons were extracted from the WAAM plates by means of water jet cutting, with the longitudinal axis of each coupon perpendicular to the deposition direction. The WAAM material was examined in both the as-built and machined (using a slitting saw) conditions, as shown in Fig. 2 (a), to investigate the influence of the inherent geometric undulations on the resulting mechanical and fatigue properties. All as-built coupons were sandblasted with glass beads with an average size of 0.16 mm, which was sufficiently coarse to clean the surface but fine enough not to affect their geometry. The edges of the fatigue coupons were finished by longitudinal polishing with grade 400 sandpaper [51]. Typical static and fatigue as-built coupons are shown in Fig. 2 (b), where the coupon dimensions, determined according to EN ISO 6892-1 [52] and EN 6072 [51], respectively, are also presented. Note that the grip sections of the fatigue coupons were longitudinally extended (from 30 mm to 60 mm) to fit in the testing machine; this also facilitated aligning specimens with their fixtures, reducing bending stresses arising from misalignment [53]. The coupon labelling system begins with the type of test (S = static; F = fatigue), followed by the type of specimen (AB = as-built; M = machined) and a number to identity each coupon.

2.2. Geometric properties

The as-built geometric properties of the WAAM coupons were examined before testing. 3D laser scanning was employed for the digital capture of the geometries of all coupons and was performed using a Faro ScanARM – see Fig. 3. The scan data for each specimen were first converted from cloud points to a polygon object using Geomagic Wrap [54], whereby the volume of the specimen was obtained and verified against a corresponding Archimedes' measurement (with volume differences within 3%). The scan model was then saved as a STL file and imported into Rhino 3D [55], in which a set of operations was conducted for further geometric analysis, including aligning the model with the global coordinate system, contouring the model along the longitudinal direction (i.e. the global x axis – see Fig. 4) and extracting grid points from the contours. A typical coupon processed in Rhino 3D is presented in Fig. 4, where only a limited number of contours and grid points are shown for illustrative purposes. For each contour, the cross-sectional area A_i, the average thickness t_i and the deviations of the cross-sectional centroid from the overall centroid of the coupon $e_{y,i}$ and $e_{z,i}$ (along the global y and z axes respectively) were calculated, while the distance between the top and bottom surface grid points was taken as the individual thickness measurement t_{ij}. A contour spacing of 0.1 mm was taken along both the x and y axes (i.e. $dx = dy = 0.1$ mm), as adopted in [13,18], to achieve both accuracy and computational efficiency.

The surface profiles of the WAAM specimens can be described by three main characteristic parameters: waviness, thickness deviation and roughness. The waviness is reflected by the eccentricities of the cross-sectional centroids in the z direction (i.e. $e_{z,i}$) along the lengths of the coupons. The thickness deviation can be represented by the standard deviation of the measured individual thicknesses t_{ij} or average cross-sectional thicknesses t_i, denoted by t_{sd} and $t_{c,sd}$, respectively. Roughness is quantified by the deviations in the direction of the normal vector

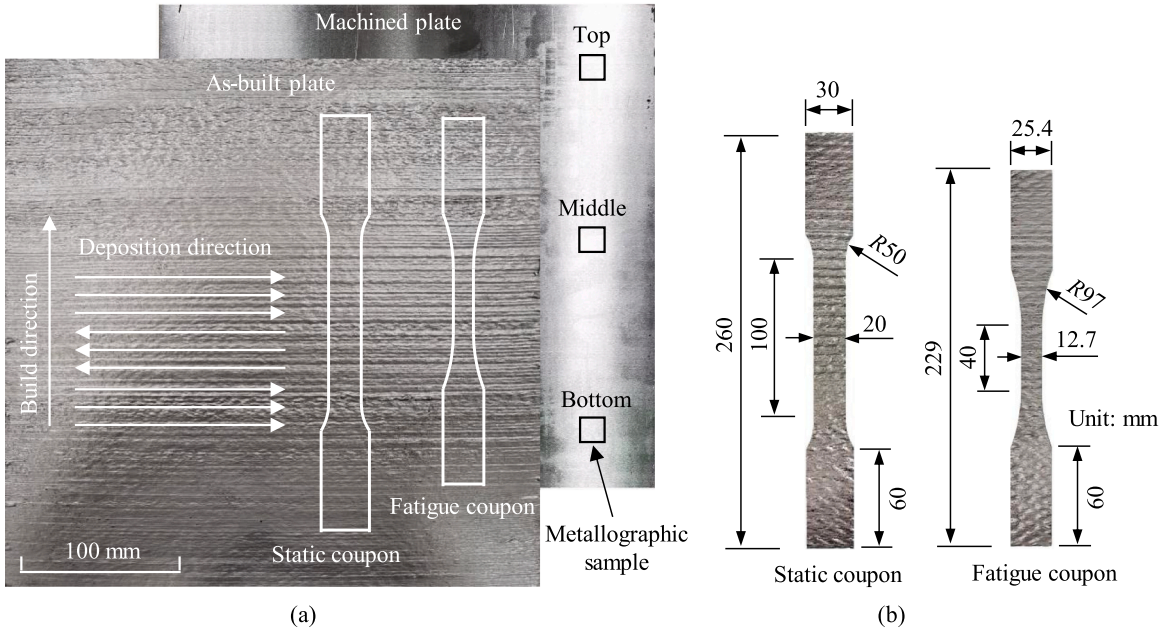

Fig. 2. (a) As-built and machined plates, deposition strategy of WAAM plates and extraction of coupons and metallographic samples; (b) typical static and fatigue as-built coupons and their nominal dimensions.

Table 1
Process parameters used for WAAM plates.

Process parameters	Details
Travel speed (mm/s)	8
Wire feed rate (m/min)	3
Welding voltage (V)	14.8
Welding current (A)	54
Gas flow rate (L/min)	14
Welding mode	Short-arc welding
Shielding gas	80% Ar + 20% CO_2
Dwell time (s)	30

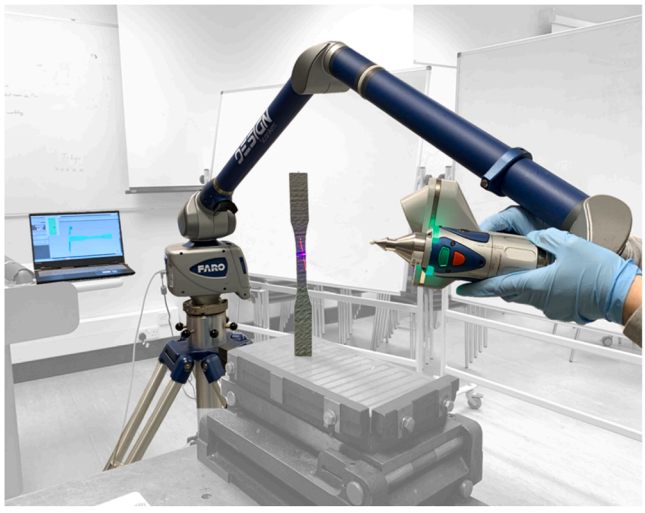

Fig. 3. Laser scanning of a typical fatigue coupon.

of a real surface from its ideal form, and was determined herein following the procedure illustrated in Fig. 5, which involved first filtering of the waviness and thickness deviation along the coupon length. The filtered surface profiles can be characterised statistically using a series of roughness parameters, including the maximum roughness R_{max}, mean arithmetic height R_a, mean square height R_q, skew R_{sk} and kurtosis R_{ku}, as given by:

$$R_{max} = z_{max}(x,y) - z_{min}(x,y) \tag{1}$$

$$R_a = \frac{1}{S}\iint_S |z(x,y)|dxdy \tag{2}$$

$$R_q = \sqrt{\frac{1}{S}\iint_S z^2(x,y)dxdy} \tag{3}$$

$$R_{sk} = \frac{1}{R_q^3}\left(\frac{1}{S}\iint_S z^3(x,y)dxdy\right) \tag{4}$$

$$R_{ku} = \frac{1}{R_q^4}\left(\frac{1}{S}\iint_S z^4(x,y)dxdy\right) \tag{5}$$

where $z(x,y)$ is the coordinates of the grid points along the thickness direction and S denotes the surface area. The geometric properties of the as-built static and fatigue coupons, including the surface roughness parameters (R_{max}, R_a, R_q, R_{sk}, R_{ku}), are summarised in Table 2, where A, A_{min} and A_{sd} and t, t_{min} and t_{sd} are the mean, minimum and standard deviation values of the cross-sectional area and thickness, respectively, and $e_{y,max}$ and $e_{z,max}$ are the maximum centroid eccentricities along the y and z axes, respectively.

2.3. Mechanical properties and microstructure

Tensile coupon tests were conducted in accordance with EN ISO 6892-1 [52] to investigate the stress-strain response of the WAAM material and hence to facilitate the determination of stress levels for the subsequent fatigue tests. Two machined and two as-built tensile coupons were tested, to assess the influence of the surface undulations on the resulting mechanical properties. Digital image correlation (DIC) was used to monitor the evolution of deformations and strains of the specimens during testing. Average stress-strain curves were derived from the applied load and DIC data, with the average stress taken as the applied load divided by the average cross-sectional area and the average strain determined over the full parallel length of each coupon. The detailed

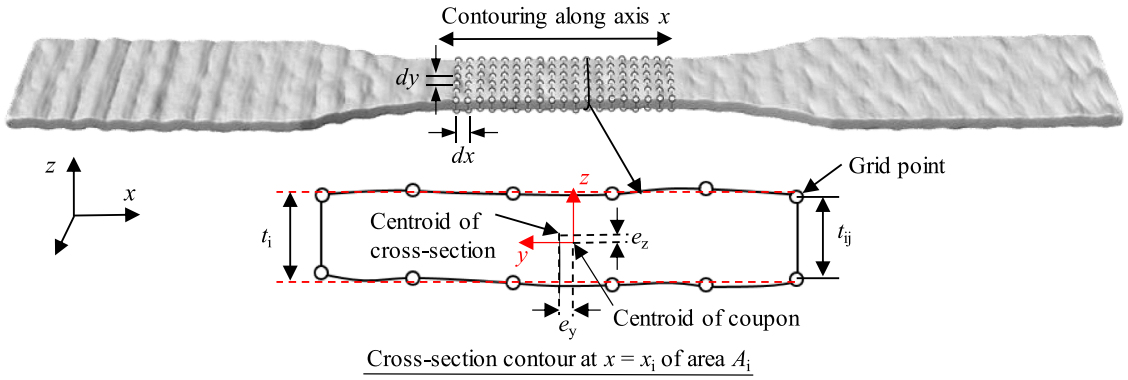

Fig. 4. Typical scan model of fatigue coupon processed in Rhino 3D.

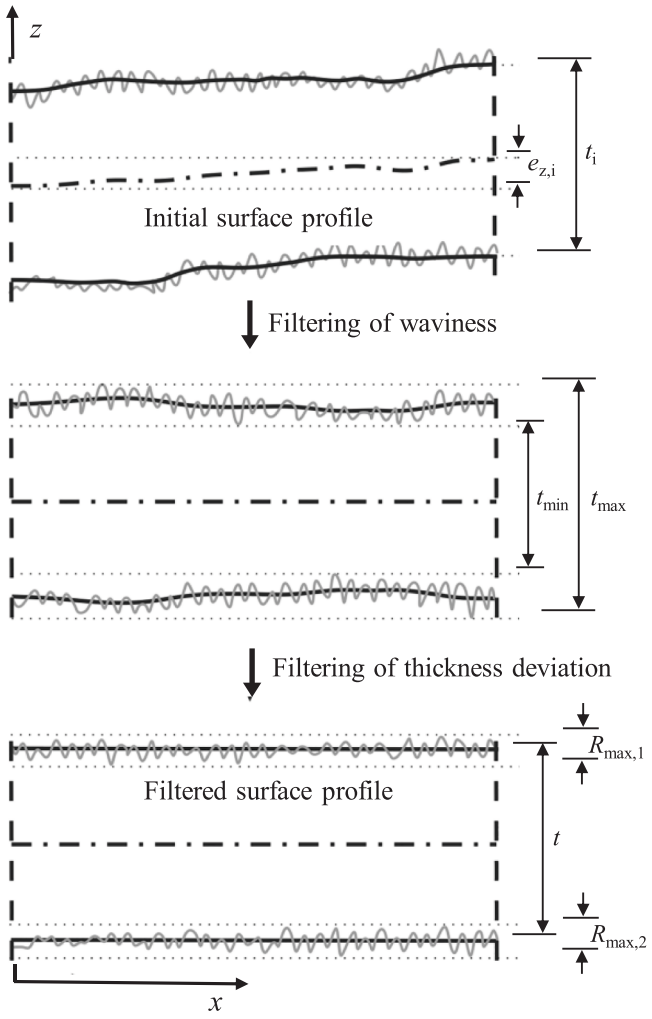

Fig. 5. Determination of surface roughness of WAAM specimens after filtering waviness and thickness deviation [43].

testing procedure and data processing have been described in [18], while the key test results are reported in this section. The measured stress-strain curves of the machined and as-built WAAM steel are plotted in Fig. 6. The examined coupons are shown to exhibit a stress-strain response featuring a sharply defined yield point, a yield plateau and subsequent strain hardening, in line with that of hot-rolled steels [2]. The overall form of the stress-strain curves of the as-built coupons is slightly different from that of the machined coupons, with the yield plateau being somewhat inclined or even fully eroded, attributed to the surface undulations resulting in some cross-sections of the coupons yielding before others. The key mechanical properties are summarised in Table 3, including the Young's modulus E, yield strength f_y, ultimate tensile strength f_u, ultimate tensile strain ε_u, fracture strain ε_f (determined over the full parallel length (100 mm) of each coupon) and the Poisson's ratio in the elastic range ν. Note that the mechanical properties of the as-built material were determined based on the average cross-sectional areas within the parallel lengths of the coupons, and that these should be considered as 'effective' properties given their dependence on the degree of geometric undulation.

In parallel with the mechanical testing, the microstructure of the WAAM steel was also examined through optical microscopy. Metallographic samples were extracted at different locations from the parent WAAM plates (i.e. the top, middle and bottom regions – see Fig. 2 (a)), and were prepared for microscopic examination in accordance with ASTM E3-11 [56]. All examined samples revealed microstructures of similar grain morphologies, compositions and sizes. A typical micrograph taken for a sample extracted from the middle region of the WAAM plates is presented in Fig. 7, where a principally ferritic-pearlitic microstructure, featuring predominantly equiaxed grains (with an average grain size of 8.2 μm), can be observed. Such microstructure is typically displayed by conventional non-alloyed structural mild steels.

2.4. Fatigue tests

The fatigue strength of the WAAM material was examined by means of constant amplitude uniaxial fatigue testing, undertaken at room temperature in accordance with E466-21 [53]. A load-controlled tension-tension sinusoidal loading regime with different stress ranges was employed. Different stress ratios (i.e. the ratios of minimum stress to maximum stress) $R = 0.1$, 0.2, 0.3 and 0.4 were adopted to assess the influence of mean stress level on the fatigue life of the WAAM steel. Note that the stress ratios of $R = 0.1$–0.4 are among typical ratios of dead to live loads in engineering structures (e.g. steel bridges) [57], and have been widely used for fatigue testing of conventional structural steels [57, 58]. A total of 75 high-cycle fatigue tests on the as-built and machined WAAM coupons were conducted, of which eight tests (ID 69–75 in Table 4) were carried out in the Structures Laboratory at the University of Sheffield, and the remaining tests were performed using a 500 kN Walter & Bai servo-hydraulic testing machine (coupled with an 100 kN load cell – see Fig. 8) in the Structural Engineering Laboratory at Empa (Swiss Federal Laboratories for Materials Science and Technology). Similar test results on the machined coupons (loaded under similar stress ranges) were obtained from the two machines, as indicated in Table 4. Hence, the influence of the testing machines on the fatigue test results is considered to be insignificant.

Constant life diagrams (CLDs) and *S-N* (stress-life) diagrams are commonly used for the graphical presentation and analysis of fatigue test data [59]. CLDs present the stress amplitude and mean stress for a

Table 2
Geometric properties of as-built static and fatigue coupons.

Coupon	A (mm^2)	$\frac{A_{min}}{A}$	$\frac{A_{sd}}{A}$	t (mm)	$\frac{t_{min}}{t}$	$\frac{t_{sd}}{t}$	$\frac{\lvert e_y \rvert_{max}}{t}$	$\frac{\lvert e_z \rvert_{max}}{t}$	R_{max}	R_a	R_k	R_{sk}	R_{ku}
S-AB-1	56.84	0.93	0.04	2.85	0.54	0.07	0.098	0.247	1.285	0.178	0.246	-0.405	3.221
S-AB-2	56.85	0.93	0.03	2.84	0.57	0.07	0.092	0.205	1.197	0.128	0.175	0.605	4.396
F-AB-1	36.77	0.96	0.02	2.92	0.43	0.06	0.039	0.090	0.996	0.121	0.154	-0.860	3.495
F-AB-2	37.06	0.97	0.02	2.93	0.57	0.06	0.044	0.082	0.784	0.081	0.105	0.009	3.701
F-AB-3	37.21	0.95	0.02	2.94	0.53	0.05	0.076	0.099	0.994	0.124	0.149	0.206	2.739
F-AB-4	36.98	0.96	0.02	2.93	0.52	0.06	0.072	0.095	0.910	0.119	0.146	0.212	2.738
F-AB-5	37.19	0.95	0.02	2.92	0.73	0.04	0.049	0.125	0.981	0.115	0.143	0.672	3.325
F-AB-6	36.67	0.97	0.02	2.90	0.55	0.05	0.054	0.091	0.788	0.084	0.106	0.418	3.443
F-AB-7	37.23	0.95	0.02	2.94	0.55	0.06	0.071	0.062	0.946	0.103	0.129	0.033	3.042
F-AB-8	37.04	0.95	0.02	2.92	0.44	0.06	0.076	0.094	1.124	0.165	0.189	-0.346	2.007
F-AB-9	36.74	0.95	0.03	2.91	0.03	0.06	0.035	0.076	0.790	0.103	0.128	-0.517	2.966
F-AB-10	36.40	0.96	0.02	2.88	0.63	0.05	0.051	0.072	0.904	0.089	0.114	0.074	3.478
F-AB-11	36.57	0.97	0.02	2.88	0.66	0.05	0.070	0.068	0.831	0.088	0.115	-0.489	4.108
F-AB-12	36.53	0.95	0.02	2.88	0.61	0.05	0.070	0.082	0.855	0.092	0.121	-0.561	3.839
F-AB-13	37.06	0.96	0.02	2.90	0.73	0.04	0.043	0.091	0.933	0.094	0.125	-0.696	4.668
F-AB-14	36.77	0.96	0.01	2.90	0.60	0.05	0.058	0.090	0.747	0.083	0.109	-0.424	3.671
F-AB-15	36.93	0.95	0.02	2.90	0.61	0.05	0.065	0.084	0.893	0.093	0.120	-0.757	3.905
F-AB-16	36.71	0.95	0.02	2.89	0.50	0.06	0.103	0.084	1.204	0.189	0.218	0.498	2.209
F-AB-17	36.42	0.95	0.02	2.86	0.65	0.06	0.055	0.090	0.756	0.101	0.125	-0.001	2.725
F-AB-18	35.84	0.94	0.02	2.82	0.56	0.06	0.049	0.074	0.778	0.093	0.118	0.387	3.052

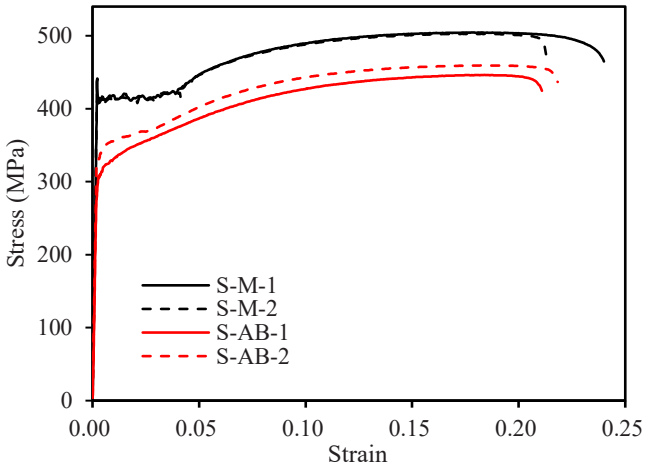

Fig. 6. Engineering stress-strain curves of machined (M) and as-built (AB) WAAM coupons.

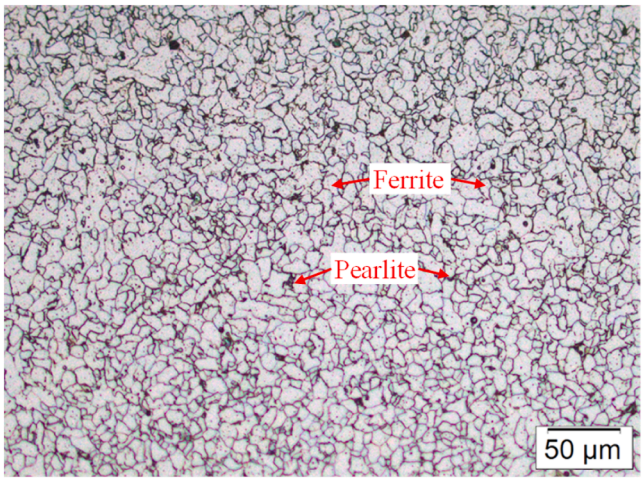

Fig. 7. Typical optical micrograph of examined WAAM steel.

Table 3
Measured material properties of machined (M) and as-built (AB) WAAM coupons.

Coupon	E (MPa)	ν	f_y (MPa)	f_u (MPa)	ε_u	ε_f
S-M-1	205700	0.26	412	504	0.18	0.24
S-M-2	207100	0.29	415	503	0.18	0.21
S-AB-1	162000	0.31	311	446	0.18	0.21
S-AB-2	179800	0.27	339	459	0.19	0.22

given fatigue life and predict the fatigue limit of a material at different stress ratios, while *S-N* diagrams describe the relationship between the stress range and number of cycles to failure. Both CLDs and *S-N* diagrams are used to analyse the obtained fatigue test data, as detailed in Sections 4 and 5, respectively. In the fatigue experiments conducted to develop the CLDs, the specimens were initially tested under a relatively low stress amplitude. If the specimens survived two million cycles, they were tested again under an increased stress level (with the same stress ratio); this procedure was repeated every two million cycles until the occurrence of fracture. On the other hand, to develop *S-N* diagrams, the specimens were fatigue-loaded until fracture or two million cycles; the latter is considered as an infinite life (i.e. run-out). Note that a subset of the test data were used in the development of both the CLDs and *S-N* diagrams, as shown in Table 4, where the test results, including the number of fatigue cycles, failure location and reason for test termination, are also presented. It can be seen from Table 4 that the majority of the coupons fractured within their parallel lengths, with fatigue cracks initiating from the edges, as illustrated in Fig. 9. Exceptions to this included as-built coupons F-AB-6, F-AB-10 and F-AB-11, where fatigue fracture occurred within the fillet or grip regions, and as-built coupons F-AB-4 and F-AB-14, where fatigue cracks initiated from the undulating surfaces, as well as a machined coupon F-M-2, where fatigue cracks originated from an internal pore – see Fig. 10. The test data for coupon F-M-2 lie within the range of those for the other machined coupons, as indicated in Table 4 and the *S-N* diagrams in Section 5, and thus, are incorporated in the subsequent fatigue analyses. Typical as-built and machined coupons after fracture are shown in Figs. 9 and 10, respectively. Note that, for the coupons (F-AB-6, F-AB-10 and F-AB-11) that fractured outside their parallel lengths, the results of the tests performed at the final (highest) stress levels (shown in Table 4) are excluded in the fatigue analyses in Sections 4 and 5.

Table 4
Summary of fatigue test results.

Test ID	Coupon	*R*	Stress range (MPa)	Frequency (Hz)	Number of cycles	Crack initiation region/failure location	Reason for termination	Use of data
1	F-AB-1	0.1	180	25	273454	Edge/near one end within parallel length	Fracture	CLDs/*S-N* diagrams
2	F-AB-2	0.1	100	25	2000000	—	Run-out	CLDs
3	F-AB-2	0.1	110	25	2000000	—	Run-out	CLDs
4	F-AB-2	0.1	120	25	2000000	—	Run-out	CLDs
5	F-AB-2	0.1	130	25	2000000	—	Run-out	CLDs
6	F-AB-2	0.1	140	25	2000000	—	Run-out	CLDs
7	F-AB-2	0.1	160	25	2000000	—	Run-out	CLDs
8	F-AB-2	0.1	180	25	2000000	—	Run-out	CLDs/*S-N* diagrams
9	F-AB-2	0.1	190	25	533440	Edge/near one end within parallel length	Fracture	CLDs/*S-N* diagrams
10	F-AB-3	0.1	160	25	2000000	—	Run-out	CLDs
11	F-AB-3	0.1	170	25	2000000	—	Run-out	CLDs/*S-N* diagrams
12	F-AB-3	0.1	180	25	296722	Edge/near one end within parallel length	Fracture	CLDs/*S-N* diagrams
13	F-AB-4	0.2	130	25	2000000	—	Run-out	CLDs
14	F-AB-4	0.2	140	25	2000000	—	Run-out	CLDs
15	F-AB-4	0.2	150	25	2000000	—	Run-out	CLDs
16	F-AB-4	0.2	160	25	2000000	—	Run-out	CLDs
17	F-AB-4	0.2	170	25	2000000	—	Run-out	CLDs
18	F-AB-4	0.2	180	25	2000000	—	Run-out	CLDs
19	F-AB-4	0.2	190	25	2000000	—	Run-out	CLDs/*S-N* diagrams
20	F-AB-4	0.2	200	25	1263410	Surface/near middle within parallel length	Fracture	CLDs/*S-N* diagrams
21	F-AB-5	0.3	120	25	2000000	—	Run-out	CLDs
22	F-AB-5	0.3	130	25	2000000	—	Run-out	CLDs
23	F-AB-5	0.3	140	25	2000000	—	Run-out	CLDs/*S-N* diagrams
24	F-AB-6	0.3	150	25	1614221	Edge/fillet, slightly beyond parallel length	Fracture	—
25	F-AB-7	0.4	120	25	2000000	—	Run-out	CLDs
26	F-AB-7	0.4	130	25	2000000	—	Run-out	CLDs
27	F-AB-7	0.4	140	25	2000000	—	Run-out	CLDs
28	F-AB-7	0.4	150	25	2000000	—	Run-out	CLDs
29	F-AB-7	0.4	160	25	2000000	—	Run-out	CLDs
30	F-AB-7	0.4	170	25	2000000	—	Run-out	CLDs/*S-N* diagrams
31	F-AB-7	0.4	180	25	434158	Edge/near one end within parallel length	Fracture	CLDs/*S-N* diagrams
32	F-AB-8	0.3	130	25	2000000	—	Run-out	CLDs
33	F-AB-8	0.3	140	25	2000000	—	Run-out	CLDs
34	F-AB-8	0.3	150	25	2000000	—	Run-out	CLDs
35	F-AB-8	0.3	160	25	2000000	—	Run-out	CLDs
36	F-AB-8	0.3	170	25	2000000	—	Run-out	CLDs
37	F-AB-8	0.3	180	25	2000000	—	Run-out	CLDs/*S-N* diagrams
38	F-AB-8	0.3	190	25	12754	Edge/near one end within parallel length	Fracture	CLDs
39	F-AB-10	0.4	150	25	2000000	—	Run-out	CLDs/*S-N* diagrams
40	F-AB-10	0.4	160	25	1343611	Edge/grip region	Fracture	—
41	F-AB-11	0.4	160	25	2000000	—	Run-out	CLDs
42	F-AB-11	0.4	170	25	2000000	—	Run-out	CLDs
43	F-AB-11	0.4	180	25	2000000	—	Run-out	CLDs/*S-N* diagrams
44	F-AB-11	0.4	190	25	1568162	Edge/fillet, slightly beyond parallel length	Fracture	—
45	F-AB-12	0.3	170	25	2000000	—	Run-out	CLDs
46	F-AB-12	0.3	180	25	2000000	—	Run-out	CLDs
47	F-AB-12	0.3	190	25	2000000	—	Run-out	CLDs/*S-N* diagrams
48	F-AB-12	0.3	200	25	666365	Edge/near one end within parallel length	Fracture	CLDs/*S-N* diagrams
49	F-AB-13	0.2	170	25	2000000	—	Run-out	CLDs/*S-N* diagrams
50	F-AB-13	0.2	180	25	1300478	Edge/near one end within parallel length	Fracture	CLDs/*S-N* diagrams

(*continued on next page*)

Table 4 (*continued*)

Test ID	Coupon	*R*	Stress range (MPa)	Frequency (Hz)	Number of cycles	Crack initiation region/failure location	Reason for termination	Use of data
51	F-AB-14	0.1	165	25	8000000	—	Run-out	CLDs/*S-N* diagrams
52	F-AB-14	0.1	200	25	1080576	Surface/near middle within parallel length	Fracture	CLDs/*S-N* diagrams
53	F-AB-15	0.1	185	25	523118	Edge/near middle within parallel length	Fracture	CLDs/*S-N* diagrams
54	F-AB-16	0.1	175	25	542935	Edge/near one end within parallel length	Fracture	CLDs/*S-N* diagrams
55	F-AB-17	0.1	195	25	8000000	—	Run-out	CLDs/*S-N* diagrams
56	F-AB-17	0.1	230	25	519303	Edge/near one end within parallel length	Fracture	CLDs/*S-N* diagrams
57	F-AB-18	0.1	220	25	859475	Edge/near one end within parallel length	Fracture	CLDs/*S-N* diagrams
58	F-M-2	0.1	340	25	331056	Pore/near middle within parallel length	Fracture	*S-N* diagrams
59	F-M-3	0.1	280	25	639900	Edge/near one end within parallel length	Fracture	*S-N* diagrams
60	F-M-4	0.1	160	25	8000000	—	Run-out	*S-N* diagrams
61	F-M-4	0.1	260	25	8000000	—	Run-out	*S-N* diagrams
62	F-M-4	0.1	360	25	165722	Edge/near one end within parallel length	Fracture	*S-N* diagrams
63	F-M-5	0.1	210	25	8000000	—	Run-out	*S-N* diagrams
64	F-M-5	0.1	370	25	177083	Edge/near one end within parallel length	Fracture	*S-N* diagrams
65	F-M-6	0.1	240	25	8000000	—	Run-out	*S-N* diagrams
66	F-M-6	0.1	320	25	2320096	—	Run-out	*S-N* diagrams
67	F-M-6	0.1	400	25	15551	Edge/near middle within parallel length	Fracture	—
68	F-M-7	0.1	202	5	2000000	—	Run-out	*S-N* diagrams
69	F-M-8	0.1	216	10	2000000	—	Run-out	*S-N* diagrams
70	F-M-8	0.1	274	8	359856	Edge/near middle within parallel length	Fracture	*S-N* diagrams
71	F-M-9	0.1	289	8	807625	Edge/near middle within parallel length	Fracture	*S-N* diagrams
72	F-M-10	0.1	290	8	483114	Edge/near middle within parallel length	Fracture	*S-N* diagrams
73	F-M-11	0.1	266	8	2000000	—	Run-out	*S-N* diagrams
74	F-M-11	0.1	287	8	509965	Edge/near middle within parallel length	Fracture	*S-N* diagrams
75	F-M-12	0.1	290	8	269005	Edge/near middle within parallel length	Fracture	*S-N* diagrams

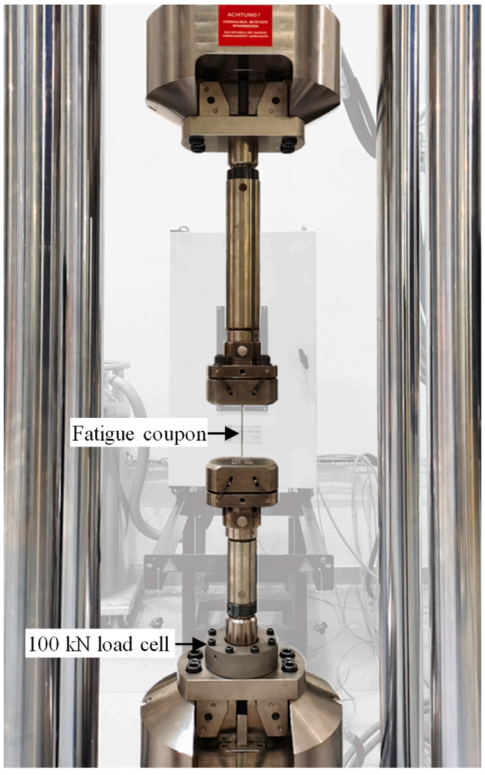

Fig. 8. Fatigue test set-up.

3. Numerical analysis

Local stress concentrations in the as-built coupons, arising from their inherent geometric irregularities, have a significant impact on their fatigue behaviour and are therefore studied by means of numerical simulations in this section. Finite element models are first developed based on the scanned geometries and measured material properties of the specimens. The static stress concentration factors of the specimens are then determined from the numerically-obtained stress distributions, after which the fatigue stress concentration factors are derived for use in the fatigue analyses in Sections 4 and 5.

3.1. Finite element modelling

Finite element (FE) simulations of the as-built coupons were performed using the FE package ABAQUS [60]. For computational efficiency, only the middle parts (i.e. the parallel lengths) of the coupons were modelled. This was achieved by trimming the scan models of the specimens in Rhino 3D [55] – see Fig. 11. Owing to the geometric irregularities of the specimens, special attention was given to the generation of a suitable finite element mesh. The surfaces of the scan models, originally characterised by an irregular triangulated mesh, were discretised with a regular quad mesh using the 'QuadRemesh' command. The resulting surfaces were closed by filling the flat faces at the ends and exported as a STEP file [61], which was then imported as a 'Part' into ABAQUS. The closed solid model (i.e. the 'Part') was then meshed in ABAQUS using tetragonal second-order elements (C3D10), with a mesh size of 0.3 mm, determined through a convergence study and also adopted in [62]. One end of the FE model was fully fixed, while the other end, where only longitudinal displacement was allowed, was subjected to the first few cycles of the fatigue loading. The procedure of developing a finite element model from a 3D scan model is illustrated in Fig. 11.

The average mechanical properties of the machined static coupons (S-M-1 and S-M-2) were assigned to the FE models, with the elastic

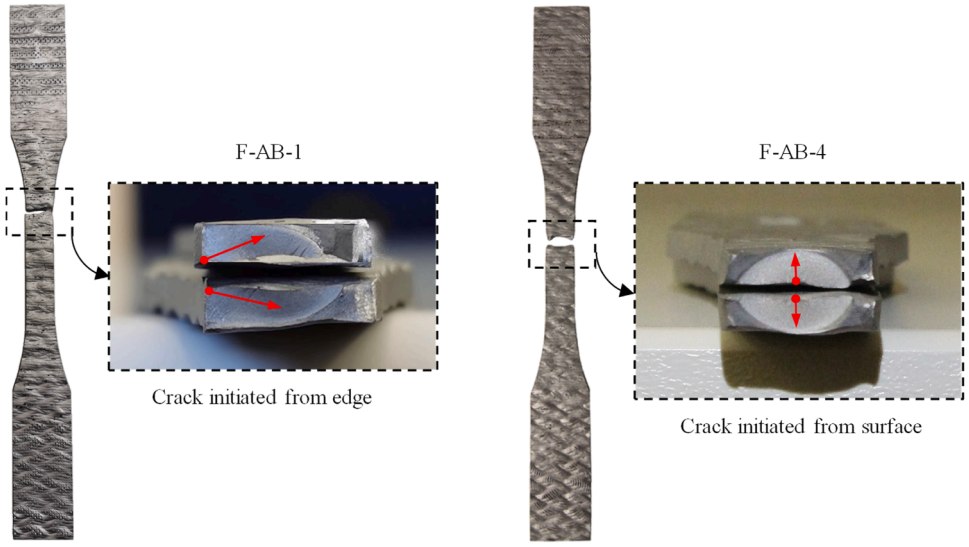

Fig. 9. Typical fractured as-built coupons and fracture surfaces.

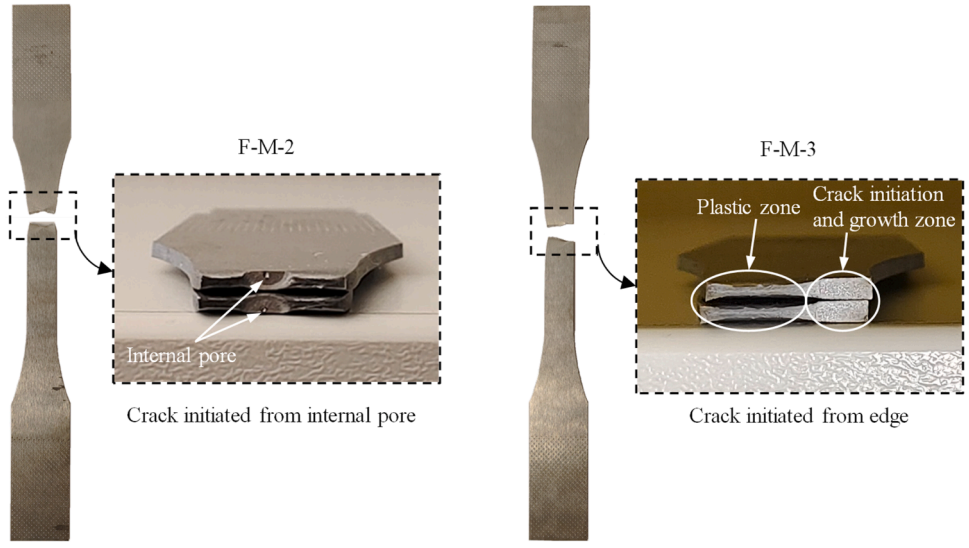

Fig. 10. Typical fractured machined coupons and fracture surfaces.

modulus, Poisson's ratio, yield stress and ultimate stress taken as $E = 206.4$ GPa, $\nu = 0.27$, $f_y = 414$ MPa and $f_u = 504$ MPa. According to the findings reported in [18], the material response of the specimens was modelled as isotropic. The full stress-strain curve used in the FE models was derived using the average measured E, f_y and f_u values (of coupons S-M-1 and S-M-2), in conjunction with the bilinear plus nonlinear hardening material model proposed by Huang et al. [2] for machined WAAM normal-strength steels. The obtained engineering stresses σ and strains ε were then converted to true stresses σ_{true} and true plastic strains ε^{pl}_{true} according to Eqs. (6) and (7) for input into ABAQUS, as given in Table 5. The established FE models were validated through comparisons between the simulated and measured stress-strain curves.

$$\sigma_{true} = \sigma(1+\varepsilon) \tag{6}$$

$$\varepsilon^{pl}_{true} = \ln\left(1+\varepsilon\right) - \frac{\sigma_{true}}{E} \tag{7}$$

3.2. Static stress concentration factors

The as-built WAAM coupons were prone to local stress concentrations during testing owing to their geometric irregularities. Stress concentration factors were hence determined to relate the local stresses σ_{loc} at the geometric discontinuities in the coupons to the nominal stresses σ_{nom}. The well-known theoretical or geometric stress concentration factors K_t [63], as given by Eq. (8), which apply to scenarios where plastic deformations are not expected to occur (e.g. ideal elastic materials) and depend on the geometries of objects and the loading conditions, were used for the coupons in which the material remained within the linear elastic range during testing.

$$K_t = \sigma_{loc}/\sigma_{nom} \tag{8}$$

However, according to the FE analysis described in Section 3.1, the peak stresses in some coupons exceeded the elastic range of the material; for these coupons, the peak stresses are denoted σ'_{loc} and effective stress concentration factors K_e, as given by Eq. (9), were adopted, the concept of which was first introduced by Peterson [63] for ductile materials.

$$K_e = \sigma'_{loc}/\sigma_{nom} \tag{9}$$

Effective stress concentration factors K_e are dependent upon both the geometric and material properties of objects, and were determined for

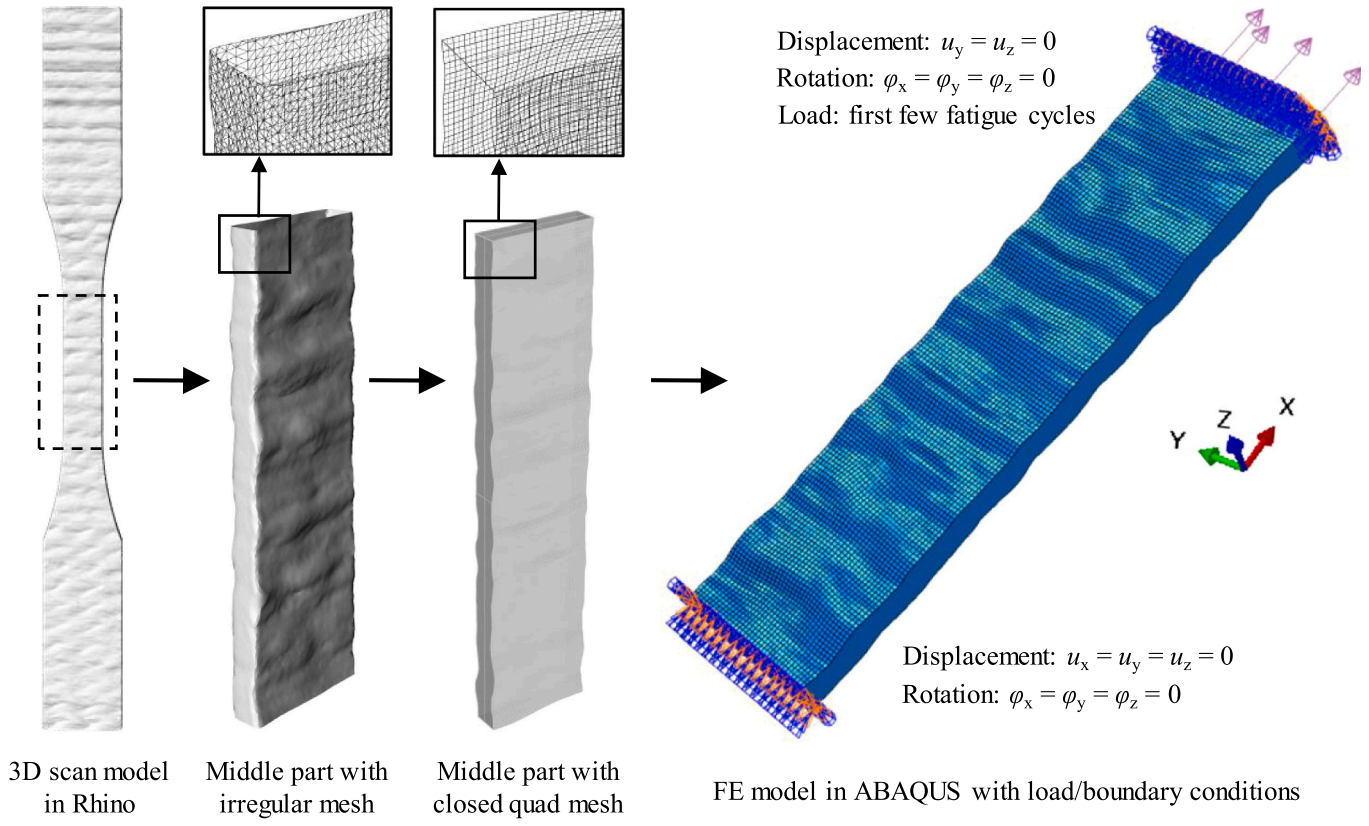

Fig. 11. Development of a finite element model from a 3D scan model.

Table 5
True stress-plastic strain data input into FE models.

True stress (MPa)	413.9	439.0	477.6	517.6	546.1	579.0	601.8
True plastic strain	0.000	0.038	0.051	0.076	0.101	0.140	0.178

the as-built WAAM coupons through the above non-linear FE analysis, which accounted for stress redistributions after material yielding. Note that, for the cases in which no local plasticity occurs, the effective stress concentration factor K_e is the same as the theoretical stress concentration factor K_t. For consistency and simplicity, K_e and K_t are both termed static stress concentration factors K_s herein.

The FE analysis showed that, owing to the surface undulations, the as-built coupons experienced multi-axial cyclic stresses, with the uniaxial tension-tension stresses being predominant and all stress components ascending and descending simultaneously, as illustrated in Fig. 12. In such cases, von Mises equivalent stresses can be employed to represent the multi-axial stress states of the coupons [64–66]. Since the fatigue damage of steels is governed by local plastic deformations [64], the use of von Mises stresses is considered to be appropriate, and has been shown previously to describe well the fatigue behaviour of ductile materials [67]. The highest von Mises equivalent stress in the FE models was therefore used to locate the fatigue critical region of each coupon. The static stress concentration factor K_s was then determined through the nominal and local stress ranges, $\Delta\sigma_{nom}$ and $\Delta\sigma_{loc}$, at the critical location (i.e. a single integration point) using:

$$K_s = \Delta\sigma_{loc}/\Delta\sigma_{nom} \tag{10}$$

The obtained static stress concentration factors are summarised in Table 6. A typical simulated distribution of von Mises stresses in coupon F-AB-4 is shown in Fig. 12 (a), highlighting the critical point C (with the maximum von Mises stress), while the evolution of the local stress σ_{loc} (i.e. the von Mises stress) at point C, alongside the cyclic nominal stress σ_{nom}, is presented in Fig. 12 (b), from which $\Delta\sigma_{nom}$ and $\Delta\sigma_{loc}$ can be determined. Note that the flattened peak of the sinusoidal local stress curve in Fig. 12 (b) is attributed to local plasticity occurring at the peak load in the first cycle, while near the valley loads, the critical region underwent negative stress components to deform compatibly with its surrounding material, resulting in the flattened valleys in the cyclic von Mises stress curve. After the first cycle, a new yielding surface was generated at the critical point, leading to the point remaining within the elastic range in the following cycles. Since no hysteretic properties have been incorporated in the FE models, the cyclic stress pattern remains consistent from the second cycle on, as shown in Fig. 12 (b).

3.3. Fatigue stress concentration factors

The obtained static stress concentration factors K_s are converted to fatigue stress concentration factors K_f by considering the notch sensitivity of the material to fatigue damage in this section. Fatigue stress concentration factors, also known as fatigue notch factors, are often used to express the reduction in the fatigue strength of a specimen due to the presence of a notch or other stress raisers. The fatigue limit of a notched specimen can be predicted to be the fatigue limit of an un-notched specimen divided by K_f. Note that the fatigue stress concentration factor K_f is typically smaller than the static stress concentration factor K_s, due to materials being not fully sensitive to the presence of notches [68]. The relationship between K_f and K_s is given by:

$$K_f = 1 + q(K_s - 1) \tag{11}$$

where q is a notch sensitivity factor [69], which can be determined by:

$$q = \frac{1}{1 + \sqrt{a/r}} \tag{12}$$

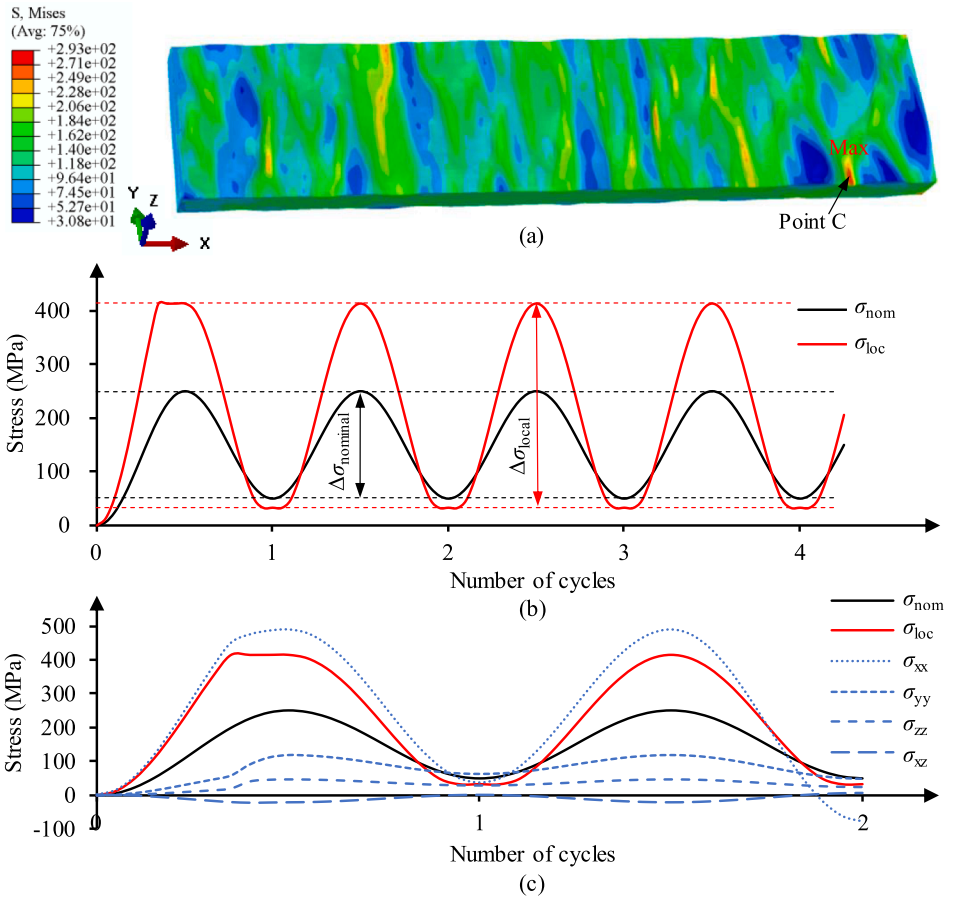

Fig. 12. (a) Distribution of von Mises stresses over coupon F-AB-4 at mean stress; (b) cyclic nominal stress (i.e. applied stress along the global *x* axis) and evolution of local stress (i.e. von Mises stress) at critical point C and (c) evolution of longitudinal (σ_{xx}), transverse (σ_{yy}), out-of-plane (σ_{zz}) and shear (σ_{xz}) stress components at point C.

Table 6
Static and fatigue stress concentration factors K_s and K_f for as-built fatigue coupons determined from FE models.

Coupon	K_s	K_f
F-AB-1	1.973	1.770
F-AB-2	1.933	1.739
F-AB-3	2.034	1.819
F-AB-4	1.907	1.718
F-AB-5	2.280	2.013
F-AB-6	2.468	2.162
F-AB-7	1.897	1.710
F-AB-8	1.748	1.592
F-AB-10	1.842	1.667
F-AB-11	1.698	1.552
F-AB-12	1.742	1.587
F-AB-13	1.767	1.607
F-AB-14	1.933	1.739
F-AB-15	1.919	1.728
F-AB-16	2.064	1.843
F-AB-17	1.874	1.692
F-AB-18	1.789	1.625

with *r* being the notch radius (in inches), which was derived herein from the laser scans and taken as 0.1 inches for all as-built coupons herein, and *a* being a material constant, which can be determined using the material tensile strength f_u (in kpsi) from:

$$\sqrt{a} = 0.246 - 3.08 \times 10^{-3} f_u + 1.51 \times 10^{-5} {f_u}^2 - 2.67 \times 10^{-8} {f_u}^3 \quad (13)$$

According to Eqs. (9)-(11), the fatigue stress concentration factors of the as-built coupons have been determined – see Table 6, and are used to calculate the local stresses for the fatigue analyses in Sections 4 and 5 using:

$$\sigma_{loc} = K_f \sigma_{nom} \quad (14)$$

4. Fatigue analysis using constant life diagrams

One of the aims of the present study is to predict the fatigue limit of WAAM steel under different stress ratios. This is of practical importance since WAAM steels may be used in highly prestressed states (e.g. due to residual stresses), and subjected to cyclic service loads with large stress ratios. Constant life diagrams (CLDs) are therefore employed to predict the fatigue strength of the examined WAAM steel, allowing for the combined effect of stress ranges and mean stress levels. In this section, following an introduction to the principle of CLDs, the fatigue test results are assessed accordingly.

4.1. Principle of constant life diagrams

Cyclic stresses are typically assumed to vary sinusoidally with time, with the alternating stress (or stress amplitude) σ_a expressed by:

$$\sigma_a = \frac{\sigma_{max} - \sigma_{min}}{2} \quad (15)$$

and the mean stress σ_m expressed by:

$$\sigma_m = \frac{\sigma_{max} + \sigma_{min}}{2} \quad (16)$$

where σ_{max} and σ_{min} are the maximum and minimum stresses in the sinusoidal stress pattern, respectively. The stress ratio is defined by:

$$R = \sigma_{min}/\sigma_{max} \tag{17}$$

Fig. 13 shows a typical constant life diagram (CLD), which comprises three main stress regions – the tension-compression ($R < 0$), compression-compression ($R > 1$) and tension-tension ($0 < R < 1$) stress regions, and three common failure criteria – the yield criterion, Goodman criterion and Gerber criterion, as given by Eqs. (16)-(18), respectively:

$$\sigma_a + \sigma_m = f_y \tag{18}$$

$$\frac{\sigma_a}{S_e} + \frac{\sigma_m}{f_u} = 1 \tag{19}$$

$$\frac{\sigma_a}{S_e} + \left(\frac{\sigma_m}{f_u}\right)^2 = 1 \tag{20}$$

where f_y and f_u are material yield strength and tensile strength, respectively, and S_e is the fatigue endurance limit (below which no fatigue failure will occur after an infinite number of load cycles – taken as two million cycles herein), and can be determined using the Marin equation [68]:

$$S_e = k_a k_b k_c k_d k_e S_e' \tag{21}$$

where k_a, k_b, k_c, k_d and k_e are the surface condition, size, load, temperature and reliability modification factors, respectively, taken as $k_a = 0.93$, $k_b = 1$, $k_c = 0.85$, $k_d = 1$ and $k_e = 1$ herein according to the recommendations in [57], S_e' is the fatigue endurance limit determined from rotary-beam tests ($R = -1$) and has been taken herein as $0.5f_u$, as recommended in [58].

These failure criteria (Eqs. (18)-(20)) reflect the typical trend of decreasing fatigue strength with increasing mean stress for conventional structural steels, and are used to assess the fatigue performance of WAAM steel in Section 4.2. The levels of the fatigue failure probability for conventional steels, as suggested by Ghafoori et al. [57,58], are also illustrated by different markers in the CLD in Fig. 13. The green triangle marker indicates the safe zone (i.e. the blue region), in which no fatigue cracks initiate. The yellow square marker indicates the risky zone, where fatigue cracks may form. The red circular marker reflects the unsafe zone, featuring a high probability of macro crack formation.

Combining Eq. (19) or Eq. (20) with Basquin's equation [70], as given by Eq. (22), the fatigue strength S_f for a given fatigue life N can be determined.

$$S_f = aN^b \tag{22}$$

where a and b are material constants, as given by Eqs. (23) and (24), respectively, for conventional mild steels:

$$a = \frac{(0.9f_u)^2}{S_e} \tag{23}$$

$$b = -\frac{1}{3}\log\left(\frac{0.9f_u}{S_e}\right) \tag{24}$$

4.2. Fatigue assessment of WAAM steel

The fatigue test results are assessed using CLDs in this section, based on both nominal stresses and local stresses. The assessment using the nominal stresses (i.e. the stresses calculated based on the average cross-sectional areas within the parallel lengths of the fatigue coupons) is illustrated in Fig. 14, where the nominal alternating stresses $\sigma_{a,nom}$ and mean stresses $\sigma_{m,nom}$ of the specimens, covering four stress ratios (R = 0.1, 0.2, 0.3 and 0.4), are presented; the green square markers represent specimens surviving beyond two million cycles, while the red triangular markers represent those failing within two million cycles. It can be observed from Fig. 14 that the fatigue strength of the as-built WAAM steel (for two million cycles) is largely insensitive to the mean stress levels, with the nominal stress amplitude remaining at about 85 MPa under the different stress ratios; this trend differs from that of decreasing fatigue strength with increasing mean stress typically associated with conventional rolled steels, but is commonly observed for steel welded joints, which often feature high levels of residual stresses [71]. Further fatigue test data over a wider range of stress ratios (e.g. $R = -1$, 0 and 0.5) are nonetheless considered necessary to confirm the findings. Note that the specimens are assumed to be loaded within the elastic range in this fatigue analysis based on nominal stresses. However, given the high stress levels imposed on a few of the as-built coupons and the stress concentration effects, local plasticity occurred (at the geometric discontinuities) on the surfaces of some specimens. An assessment of the fatigue test data based on the local stresses in the as-built coupons has therefore been carried out, as described below.

The local alternating stresses $\sigma_{a,loc}$ and local mean stresses $\sigma_{m,loc}$ (i.e. the nominal stress values multiplied by the corresponding fatigue stress concentration factors in Table 6) in the WAAM coupons are plotted in a

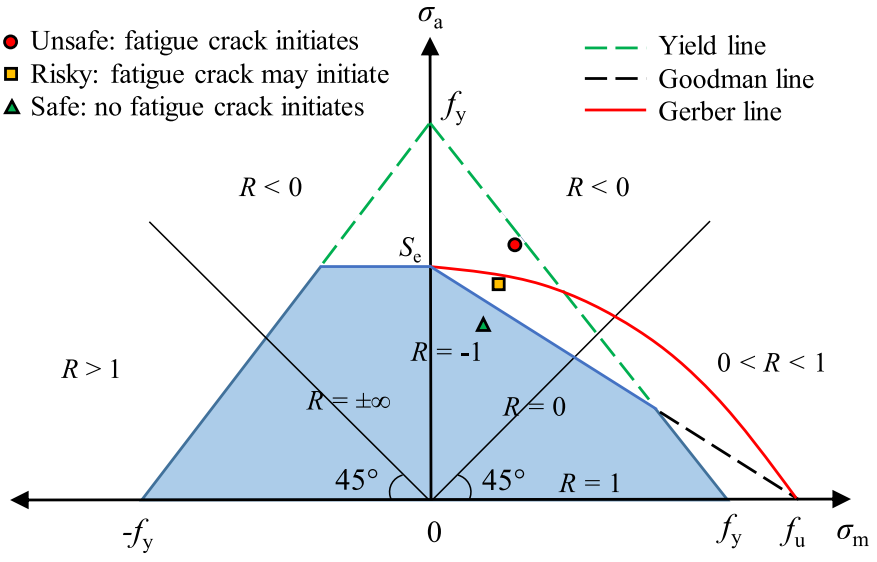

Fig. 13. Typical constant life diagram with different fatigue failure criteria and zones [57,58].

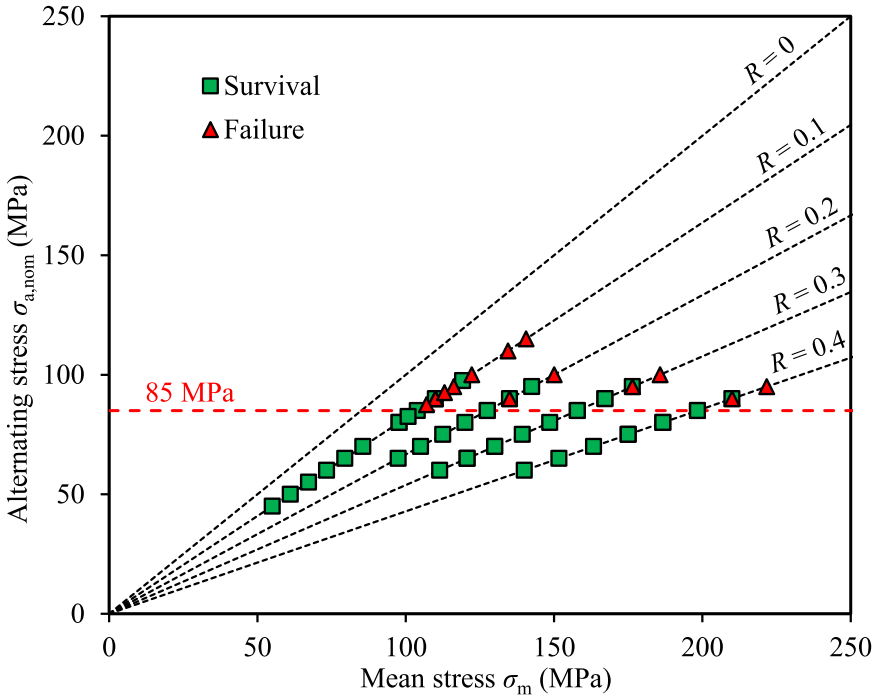

Fig. 14. Assessment of fatigue test results in a CLD based on nominal stresses.

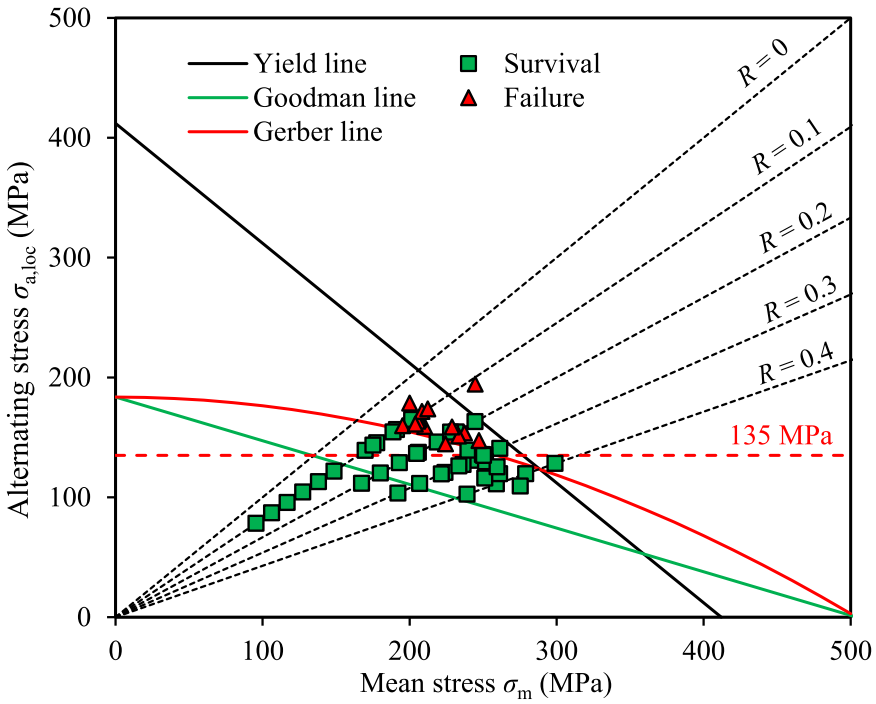

Fig. 15. Assessment of fatigue test results in a CLD based on local stresses.

CLD in Fig. 15, where the yield, Goodman and Gerber failure criteria (Eqs. (18)-(20)) are also depicted, with the material yield strength f_y being 413 MPa, determined from the material tests described in Section 2.3, and the fatigue endurance limit S_e being 184 MPa, determined from Eq. (21). According to the FE simulations described in Section 3, most areas of the surfaces of the as-built coupons remained elastic under the test loads, while stress concentrations resulted in the peak stress on some of the surfaces reaching yield. The material did not experience strain hardening though, since the maximum strains were found to be below 0.5% (i.e. remaining within the yield plateau region). Hence, the local mean stresses in the specimens can be approximately calculated as $\sigma_{m,loc} = \sigma_y - \sigma_{a,loc}$, and the actual values were determined from the FE simulations (see Fig. 12 (b)); the corresponding data points are shifted to the left in the CLD, leading to the local stress ratios ranging from 0.05 to 0.25 – see Fig. 15. Most data points for which fatigue failure occurred (i.e. the red triangular markers) are observed to lie slightly above the Gerber line, while those below the Gerber line are predominately the specimens that survived beyond two million cycles (i.e. the green square

markers). This indicates that, on the basis of local stresses, the Gerber criterion is generally accurate in predicting the fatigue strength of the WAAM steel under different stress ratios. In contrast, the Goodman criterion appears to be overly conservative, lying much lower than the data points of the fractured specimens. As can be seen from both Figs. 14 and 15, whether fatigue failure occurs depends primarily on σ_a rather than σ_m; hence, a fatigue limit of $\Delta\sigma = 170$ MPa and 270 MPa (i.e. $2\sigma_a$), determined based on nominal and local stresses, respectively, may be adopted for the examined WAAM steel loaded under different mean stress levels.

Substituting the local alternating and mean stresses, $\sigma_{a,loc}$ and $\sigma_{m,loc}$, of the fractured specimens into the Gerber equation (Eq. (20)), the fatigue limit S_e (i.e. the fatigue strength S_f under an equivalent fully-reversed stress state) can be determined for each specimen. The fatigue life of each fractured specimen can then be back-calculated by substituting the fatigue strength S_f into the Basquin model (Eqs. (22)-(24)). The predicted fatigue lives of the specimens are in good agreement with the test results, as illustrated in Fig. 16. It is thus demonstrated that Basquin's equation, initially established for conventional structural steels, appears to be also applicable to WAAM steel.

5. Fatigue analysis using *S-N* diagrams

S-N (stress-life) curves are widely used to represent the relationship between the stress range and fatigue life of conventional structural steels [72,73]. The basic *S-N* curve is expressed as:

$$N = CS^{-m} \tag{25}$$

which, in double logarithmic coordinates, can be expressed as:

$$\log N = \log C - m \log S \tag{26}$$

where S is the stress range (i.e. $\Delta\sigma = \sigma_{max} - \sigma_{min}$), N is the number of cycles to failure, and C and m are material constants. Note that the expression for the *S-N* curves (Eq. (25)) is essentially the same as Basquin's equation (Eq. (22)); the difference lies in that the latter features coefficients a and b established for conventional structural steels. The suitability of Eq. (22) for WAAM steels has been assessed in Section 4.2, while Eq. (25) is used to fit the fatigue data, deriving coefficients C and m by regression analysis. Note also that some of the equations presented herein (including Eqs. (12), (13), (21), (23) and (24)) were developed based mainly on statistical regression.

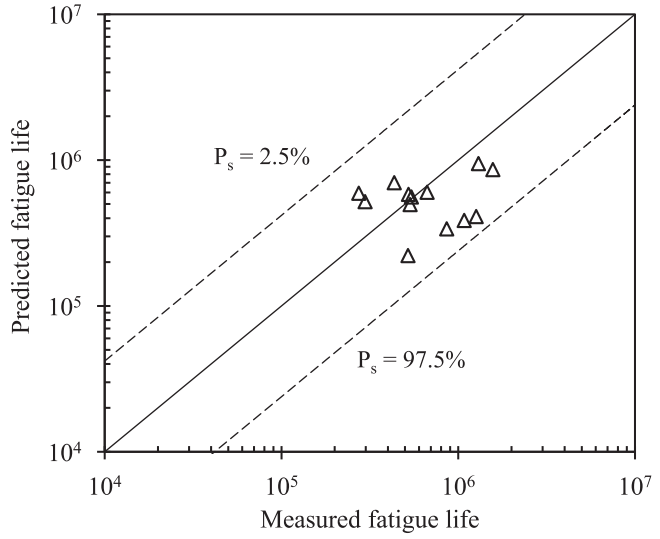

Fig. 16. Comparison of measured fatigue lives of WAAM steel with predictions from CLDs (P_s: probability of survival).

The CLDs in Section 4 have revealed a weak dependency of the fatigue strengths of the WAAM steel on the examined stress ratios. In this section, the fatigue test results are further assessed using *S-N* diagrams, with a focus on the influence of stress ranges. The stress ratios examined in the *S-N* diagrams are primarily $R = 0.1$, coupled with several other stress ratios ($R = 0.2$, 0.3 and 0.4), as shown in Table 4. The fatigue assessments are based on both the nominal stresses and local stresses of the specimens, as described in Sections 5.1 and 5.2, respectively. Subsequently, the fatigue performance of the studied WAAM steel is compared against that of butt-welded and hot-rolled steels in Sections 5.3 and 5.4, respectively.

5.1. Fatigue analysis based on nominal stresses

A fatigue assessment of the WAAM material based on the nominal stresses is presented in this section. The nominal stress ranges $\Delta\sigma_{nom}$ of the tested as-built coupons are plotted against the number of cycles to failure N in log-log coordinates in Fig. 17, where test data on the same WAAM material collected from [43] are also depicted. Eq. (26) was fitted to all test data with finite fatigue lives ($N \leq 2 \times 10^6$) in Fig. 17 by means of linear regression analysis, taking $\log(N)$ as the dependent variable; an inverse slope exponent of $m = 2.9$ was determined, which is very close to the value of $m = 3$ specified in EN 1993-1-9 [74] and the IIW Recommendations [75]. Hence, an inverse slope of $m = 3$ was also adopted for the *S-N* curves for WAAM steel fitted herein. The fitted *S-N* curve is presented in Fig. 17, together with a scatter band corresponding to probabilities of survival $P_s = 2.5\%$ and 97.5%, determined by assuming a log-normal distribution of the fatigue life N for each stress level. As can be seen from Fig. 17, the lower bound of the scatter band ($P_s = 97.5\%$) is very close to the fatigue class (FAT) of 80 MPa (i.e. a stress range at $N = 2 \times 10^6$), which is a common FAT for steel welded joints [75]. A fatigue endurance limit of 170 MPa was also derived from the *S-N* diagram, in line with that predicted by the CLD method described in Section 4.

The fatigue test results for the WAAM machined coupons, together with test data on the same material collected from [44] and [76], are assessed based on the nominal stresses in Fig. 18. Note that the fatigue data collected from [76] were obtained from ER70S-6 WAAM steel printed using the oscillatory deposition strategy (typically used to fabricate plates thicker than 20 mm [2]) rather than the more common parallel deposition strategy used in [44] and the present study; this resulted in different fatigue properties of the WAAM material, as indicated in Fig. 18, where the data in question lie above the other data; hence, the corresponding data [76] have not been considered in the following fatigue analyses. According to the *S-N* diagram, a fatigue limit of 270 MPa was derived for the machined WAAM material, as also predicted by the above CLD method. An *S-N* curve with a prescribed slope of $m = 3$ was fitted to the data with finite fatigue lives ($N \leq 2 \times 10^6$), as shown in Fig. 18, where a scatter band with $P_s = 2.5\%$ and 97.5% is also presented, with the lower bound ($P_s = 97.5\%$) approaching FAT 130. It can be observed from Figs. 17 and 18 that the scatter band for the as-built material is wider than that for the machined material, owing to the greater geometric variability.

To examine the influence of the surface undulations on the fatigue behaviour, the test results of the as-built coupons are compared with those of the machined coupons. Comparisons are made based on the nominal stresses in Fig. 19, where the fatigue test data of both machined and as-built coupons, generated herein and collected from [43,44], as well as the corresponding fitted *S-N* curves, are presented. It is clear that the as-built WAAM material exhibited inferior fatigue performance compared to the machined material, with the fatigue endurance limit reduced by about 35% due to the surface undulations. As also indicated from Fig. 19, under a given stress level (beyond the fatigue limit), the surface undulations resulted in a fatigue life about 60% shorter for the as-built WAAM material, relative to the machined material. Note that the reductions in the fatigue strengths or lives stated above are average

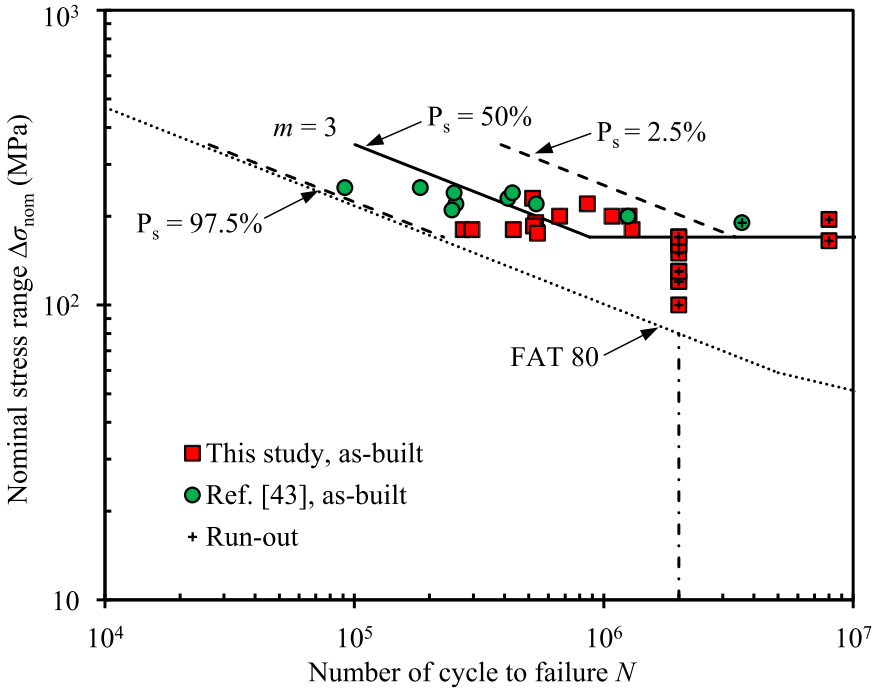

Fig. 17. Assessment of fatigue test data on as-built coupons in an *S-N* diagram based on nominal stresses.

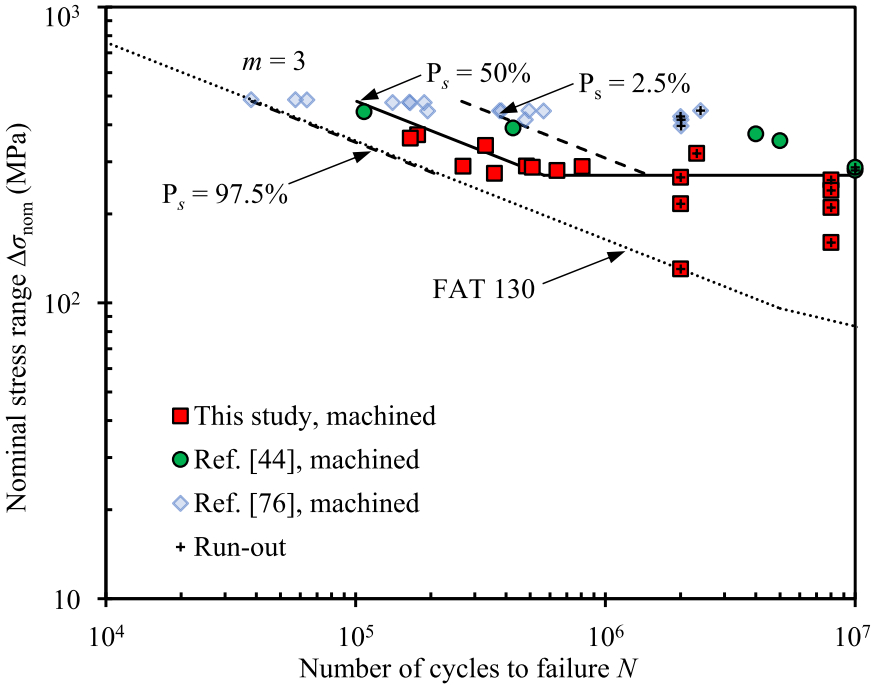

Fig. 18. Assessment of fatigue test data on machined coupons in an *S-N* diagram based on nominal stresses.

values and are determined through the fitted *S-N* curves of the as-built and machined coupons. Note also that the findings from the fatigue analysis based on nominal stresses depend largely on the printed geometries of the WAAM elements. It is therefore instructive to consider the use of local stresses for the fatigue analysis of as-built WAAM elements, which incorporate the influence of stress concentrations induced by the geometric undulations, as addressed in the next section.

5.2. Fatigue analysis based on local stresses

A fatigue assessment of the WAAM material based on the local stresses is presented in this section. The local stress ranges $\Delta\sigma_{loc}$ of both the as-built and machined coupons are plotted against the number of cycles to failure N in Fig. 20, where test data collected from [43,44] are also depicted. Note that the local stress ranges of the as-built coupons tested herein were calculated as the nominal stress ranges multiplied by the corresponding fatigue stress concentration factors K_f in Table 6 (i.e. equal to the maximum von Mises stress ranges derived from the FE

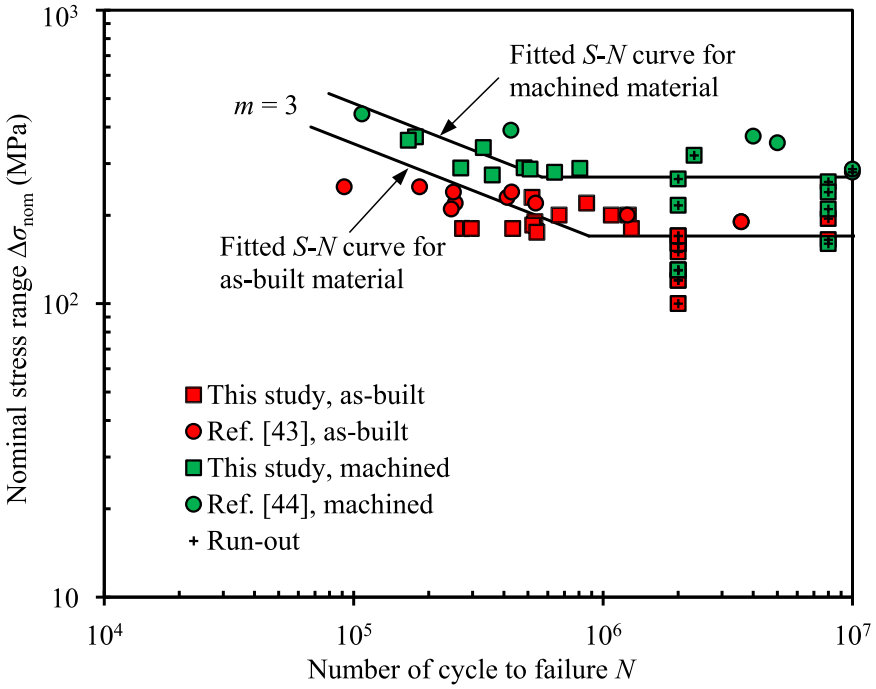

Fig. 19. Comparison of fatigue test results of as-built and machined WAAM coupons.

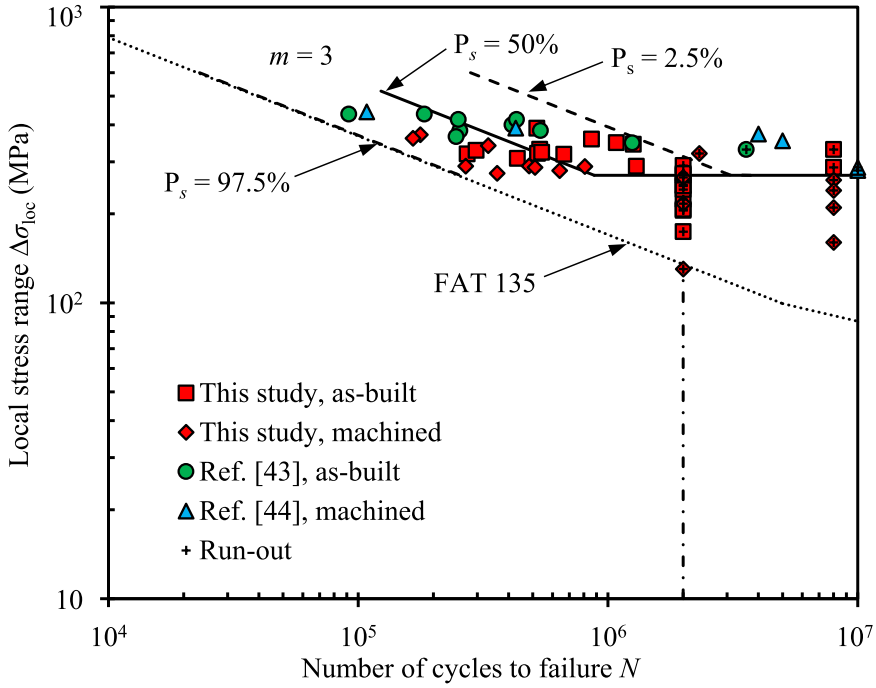

Fig. 20. Assessment of fatigue test data in an *S-N* diagram based on local stresses.

models), while for the as-built coupons tested in [43], printed using the same material in a similar manner, an average K_f of 1.74 determined from this study was used to calculate the local stress ranges. Note also that, for the machined coupons (without the geometric undulations), the local stresses are deemed to be equal to the nominal stresses. As can be seen from Fig. 20, the test data (with $N \leq 2 \times 10^6$) on the as-built coupons generally fall within the range of those on the machined coupons. This reflects the accuracy of the numerical method described in Section 3 in determining the stress concentration factors of the as-built coupons. An *S-N* curve was fitted to all test data with finite fatigue lives in Fig. 20, leading to an inverse slope of $m = 3.1$, which remains close to the recommended value of $m = 3$ in EN 1993-1-9 [74]. Hence, the linear regression was again conducted with a prescribed inverse slope of $m = 3$. The fitted *S-N* curve is presented in Fig. 20, together with a scatter band corresponding to $P_s = 2.5\%$ and 97.5%, with the lower bound ($P_s = 97.5\%$) lying very close to FAT 135. The fatigue endurance limit was determined as 270 MPa, in line with that predicted by the CLD method for the as-built material based on local stresses.

5.3. Comparisons with steel butt welds

WAAM is essentially a robotic welding process, with layers of deposited material being equivalent to conventional welds. In this section, the fatigue behaviour of the as-built WAAM material is compared against that of steel butt welds. Fatigue test results on 576 steel butt-welded joints, covering a range of material thicknesses (from 6 to 20 mm) and stress ratios (from −1 to 0.5), have been collected from [77]. The nominal stress ranges $\Delta\sigma_{nom}$ of the butt-welded joints are plotted against the number of cycles to failure N in Fig. 21, where the test data on the as-built WAAM material generated in this study and collected from [43], as well as the fitted *S-N* curve and a scatter band corresponding to $P_s = 2.5\%$ and 97.5%, are also depicted. As can be seen from Fig. 21, the majority of the butt-welded joint data (about 96%, excluding the run-out data) fall within the scatter band plotted for the WAAM steel data, indicating similar fatigue behaviour of the WAAM material to that of the butt welds. Further, the nominal stress-based fatigue class FAT 80, as commonly adopted for steel butt-welded joints in the IIW Recommendations [75], appears to be also suitable for the examined as-built WAAM steel.

5.4. Comparisons with S355 structural steel

According to the tensile tests presented in Section 2.3, the examined WAAM material is shown to exhibit similar mechanical properties to S355 hot-rolled steel. In this section, the fatigue behaviour of the WAAM material is compared with that of S355 structural steel. The fatigue test results of the examined WAAM material and those collected from [43,44], along with the corresponding scatter band, are plotted in Fig. 22, where fatigue test data on S355 steel collected from [78–83] are also presented for comparison purposes. The local stresses of the as-built WAAM material, i.e. the products of the nominal stresses and K_f, were used in the comparisons, while for the machined WAAM material and the S355 steel, the local stresses were taken as the nominal stresses. As can be seen from Fig. 22, the WAAM steel and the S355 steel data (excluding the run-out ones) generally follow the same trend and lie within a similar range, indicating comparable fatigue performance. The fatigue class FAT 135, determined based on local stresses, appears to be suitable for both the examined WAAM steel and S355 structural steel.

6. Conclusions

A comprehensive experimental study into the fatigue behaviour of WAAM plates made of ER70S-6 steel wire has been presented. A total of 75 high-cycle fatigue tests on both as-built and machined coupons, covering various stress ranges and stress ratios (R = 0.1, 0.2, 0.3 and 0.4), have been conducted. 3D laser scanning was employed to capture the geometries of the WAAM coupons, while the scan data were used in finite element models to study the local stress concentrations in the as-built coupons.

The obtained fatigue test results were assessed using constant life diagrams (CLDs) and *S-N* diagrams. Given the inherent geometric variability of WAAM, the assessments were carried out based on both nominal stresses and local stresses, with the latter determined from the numerical analyses. The CLDs revealed that the fatigue strength of the as-built WAAM steel (for two million cycles) was relatively insensitive to the mean stress levels, generally remaining at a nominal stress range of 170 MPa and a local stress range of 270 MPa under different stress ratios. The *S-N* diagrams showed that, owing to the surface undulations, the as-built WAAM material exhibited a reduction of about 35% in the fatigue endurance limit relative to the machined material, and a reduction of about 60% in the fatigue life if subjected to the same cyclic load level. According to the comparisons based on nominal and local stresses, the WAAM steel exhibited comparable fatigue performance to conventional steel butt welds and structural steel S355, respectively. Based on the fatigue test results and numerical analyses, preliminary *S-N* curves were also explored for the WAAM steel in both the machined and as-built conditions. Nominal stress-based and local stress-based fatigue classes, FAT 80 and FAT 135, with an inverse slope of $m = 3$, were found to be suitable for WAAM ER70S-6 steel, although additional test data are considered necessary for further confirmation and reliability assessment.

CRediT authorship contribution statement

Cheng Huang: Investigation, Formal analysis, Methodology,

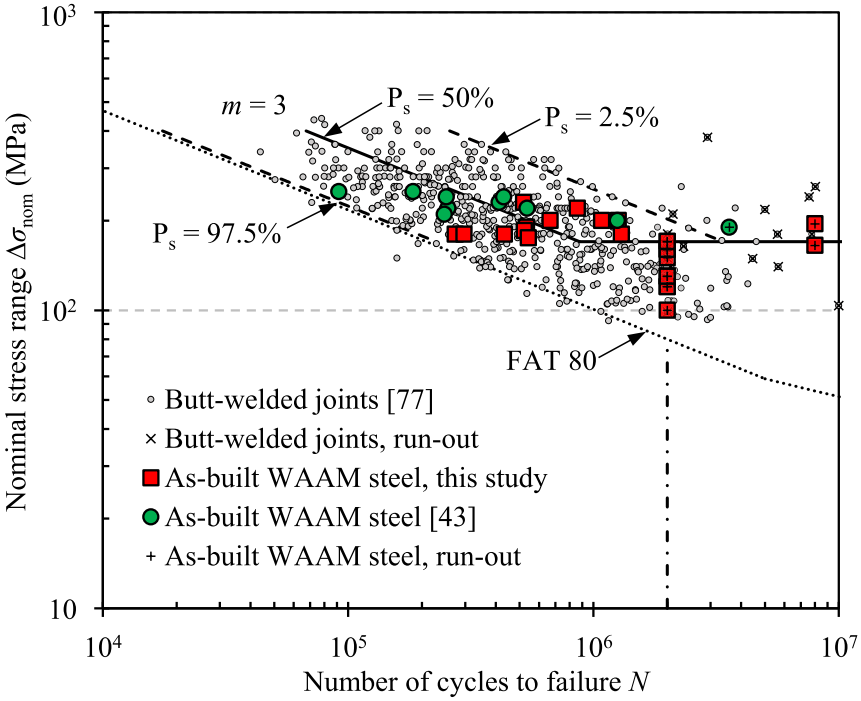

Fig. 21. Comparison of fatigue test results between WAAM material and steel butt welds.

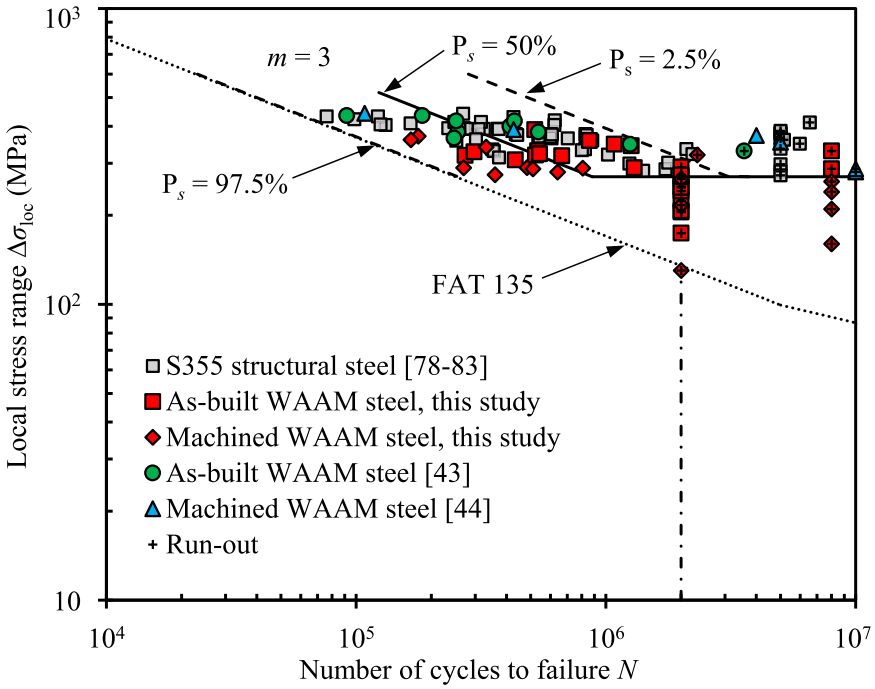

Fig. 22. Comparison of fatigue test results between WAAM material and S355 structural steel.

Writing - original draft, Writing - review & editing. **Lingzhen Li:** Investigation, Formal analysis, Methodology, Writing - original draft. **Niels Pichler:** Investigation, Formal analysis, Methodology, Writing - original draft. **Elyas Ghafoori:** Conceptualization, Methodology, Supervision, Writing - review & editing. **Luca Susmel:** Conceptualization, Supervision, Writing - review & editing. **Leroy Gardner:** Conceptualization, Supervision, Writing - review & editing.

Declaration of Competing Interest

The authors declare that they have no known competing financial interests or personal relationships that could have appeared to influence the work reported in this paper.

Data availability

Data will be made available on request.

Acknowledgements

The authors gratefully acknowledge funding and support from the China Scholarship Council (CSC). The authors also would like to acknowledge MX3D for the fabrication of the test specimens and Mr Robert Widmann and Mr Davide Ferrari for their assistance in the research.

References

[1] L. Gardner, Metal additive manufacturing in structural engineering – review, advances, opportunities and outlook, Structures 47 (2022) 2178–2193.
[2] C. Huang, P. Kyvelou, L. Gardner, Stress-strain curves for wire arc additively manufactured steels, Eng. Struct. 279 (2023), 115628.
[3] V.A. Silvestru, I. Ariza, J. Vienne, L. Michel, A.M. Aguilar Sanchez, U. Angst, et al., Performance under tensile loading of point-by-point wire and arc additively manufactured steel bars for structural components, Mater. Des. 205 (2021), 109740.
[4] T. Tankova, D. Andrade, R. Branco, C. Zhu, D. Rodrigues, L. Simões da Silva, Characterization of robotized CMT-WAAM carbon steel, J. Constr. Steel Res 199 (2022), 107624.
[5] T.A. Rodrigues, V. Duarte, R.M. Miranda, T.G. Santos, J.P. Oliveira, Current status and perspectives on wire and arc additive manufacturing (WAAM), Materials 12 (2019) 1121.
[6] N. Rodideal, C.M. Machado, V. Infante, D.F.O. Braga, T.G. Santos, C. Vidal, Mechanical characterization and fatigue assessment of wire and arc additively manufactured HSLA steel parts, Int. J. Fatigue 164 (2022), 107146.
[7] V. Mishra, A. Babu, R. Schreurs, K. Wu, M.J.M. Hermans, C. Ayas, Microstructure estimation and validation of ER110S-G steel structures produced by wire and arc additive manufacturing, J. Mater. Res. Technol. 23 (2023) 3579–3601.
[8] M. Wächter, M. Leicher, M. Hupka, C. Leistner, L. Masendorf, K. Treutler, S. Kamper, A. Esderts, V. Wesling, S. Hartmann, Monotonic and fatigue properties of steel material manufactured by wire arc additive manufacturing, Appl. Sci. 10 (2020) 5238.
[9] ASTM International. Additive manufacturing—general principles—terminology. ISO/ASTM 52900, West Conshohocken, PA. 2017.
[10] L. Gardner, P. Kyvelou, G. Herbert, C. Buchanan, Testing and initial verification of the world's first metal 3D printed bridge, J. Constr. Steel Res. 172 (2020), 106233.
[11] T. Feucht, J. Lange, M. Erven, C.B. Costanzi, U. Knaack, B. Waldschmitt, Additive manufacturing by means of parametric robot programming, Constr. Robot 4 (2020) 31–48.
[12] MX3D, Structural connector for TAKANAKA, 2019. <https://mx3d.com/industries/construction/connector-for-takenaka/> (accessed 28 May 2021).
[13] P. Kyvelou, H. Slack, D. Daskalaki Mountanou, M.A. Wadee, T.B. Britton, et al., Mechanical and microstructural testing of wire and arc additively manufactured sheet material, Mater. Des. 192 (2020), 108675.
[14] V. Laghi, M. Palermo, G. Gasparini, V.A. Girelli, T. Trombetti, Experimental results for structural design of Wire-and-Arc Additive Manufactured stainless steel members, J. Constr. Steel Res. 167 (2020), 105858.
[15] P. Kyvelou, C. Huang, L. Gardner, C. Buchanan, Structural testing and design of wire arc additively manufactured square hollow sections, J. Struct. Eng. 147 (2021) 1–19.
[16] C. Huang, X. Meng, L. Gardner, Cross-sectional behaviour of wire arc additively manufactured tubular beams, Eng. Struct. 272 (2022), 114922.
[17] C. Huang, X. Meng, C. Buchanan, L. Gardner, Flexural buckling of wire arc additively manufactured tubular columns, J. Struct. Eng. 148 (2022) 04022139.
[18] C. Huang, P. Kyvelou, R. Zhang, T.B. Britton, L. Gardner, Mechanical testing and microstructural analysis of wire arc additively manufactured steels, Mater. Des. 216 (2022), 110544.
[19] V. Laghi, M. Palermo, G. Gasparini, V.A. Girelli, T. Trombetti, On the influence of the geometrical irregularities in the mechanical response of Wire-and-Arc Additively Manufactured planar elements, J. Constr. Steel Res 178 (2021), 106490.
[20] Das A.K. Metallurgy of failure analysis. McGraw Hill Professional, 1997.
[21] S. Rahmati, Direct rapid tooling. Compr. Mater. Process. 10 (2014) 303–344.
[22] T. Chen, C. Huang, Fatigue tests on edge cracked four-point bend steel specimens repaired by CFRP, Compos Struct. (2019) 219.
[23] C. Huang, T. Chen, S. Feng, Finite element analysis of fatigue crack growth in CFRP-repaired four-point bend specimens, Eng. Struct. 183 (2019) 398–407.
[24] T. Chen, C. Huang, L. Hu, X. Song, Experimental study on mixed-mode fatigue behavior of center cracked steel plates repaired with CFRP materials, Thin-Walled Struct. 135 (2019) 486–493.

[25] H. Xin, J.A.F.O. Correia, M. Veljkovic, Three-dimensional fatigue crack propagation simulation using extended finite element methods for steel grades S355 and S690 considering mean stress effects, Eng. Struct. 227 (2021), 111414.
[26] E. Ghafoori, H. Dahaghin, C. Diao, N. Pichler, L. Li, M. Mohri, J. Ding, S. Ganguly, S. Williams, Fatigue strengthening of damaged steel members using wire arc additive manufacturing, Eng. Struct. 284 (2023), 115911.
[27] T. Chen, C. Yao, L. Hu, et al., Numerical analysis of central mixed-mode cracking in steel plates repaired with CFRP materials, Thin-Walled Struct. 143 (2019), 106196.
[28] C. Cui, A. Chen, R. Ma, B. Wang, S. Xu, Fatigue life estimation for suspenders of a three-pylon suspension bridge based on vehicle-bridge-interaction analysis, Materials 12 (2019) 2617.
[29] Y. Li, Y. Yuan, D. Wang, S. Fu, D. Song, M. Vedani, X. Chen, Low cycle fatigue behavior of wire arc additive manufactured and solution annealed 308 L stainless steel, Addit. Manuf. 52 (2022), 102688.
[30] A. Sales, A. Kotousov, L. Yin, Design against fatigue of super duplex stainless steel structures fabricated by wire arc additive manufacturing process, Metals 11 (2021) 1965.
[31] J.V. Gordon, C.V. Haden, H.F. Nied, R.P. Vinci, D.G. Harlow, Fatigue crack growth anisotropy, texture and residual stress in austenitic steel made by wire and arc additive manufacturing, Mater. Sci. Eng. A 724 (2018) 431–438.
[32] R. Duraisamy, S.M. Kumar, A.R. Kannan, N.S. Shanmugam, K. Sankaranarayanasamy, Fatigue behavior of austenitic stainless steel 347 fabricated via wire arc additive manufacturing, J. Mater. Eng. Perform. 30 (2021) 6844–6850.
[33] J. Gordon, J. Hochhalter, C. Haden, D.G. Harlow, Enhancement in fatigue performance of metastable austenitic stainless steel through directed energy deposition additive manufacturing, Mater. Des. 168 (2019), 107630.
[34] H. Xin, J.A.F.O. Correia, M. Veljkovic, Y. Zhang, F. Berto, A.M.P. de Jesus, Probabilistic strain-fatigue life performance based on stochastic analysis of structural and WAAM-stainless steels, Eng. Fail Anal. (2021) 127.
[35] A.K. Syed, X. Zhang, A. Caballero, M. Shamir, S. Williams, Influence of deposition strategies on tensile and fatigue properties in a wire + arc additive manufactured Ti-6Al-4V, Int. J. Fatigue 149 (2021), 106268.
[36] X. Wang, Y. Zhao, L. Wang, L. Wei, J. He, X. Guan, In-situ SEM investigation and modeling of small crack growth behavior of additively manufactured titanium alloy, Int. J. Fatigue 149 (2021), 106303.
[37] E. Akgun, X. Zhang, R. Biswal, Y. Zhang, M. Doré, Fatigue of wire+arc additive manufactured Ti-6Al-4V in presence of process-induced porosity defects, Int. J. Fatigue 150 (2021), 106315.
[38] J. Zhang, X. Wang, S. Paddea, X. Zhang, Fatigue crack propagation behaviour in wire + arc additive manufactured Ti-6Al-4V: Effects of microstructure and residual stress, Mater. Des. 90 (2016) 551–561.
[39] Z. Liao, B. Yang, S. Xiao, G. Yang, T. Zhu, Fatigue crack growth behaviour of an Al-Mg4.5Mn alloy fabricated by hybrid in situ rolled wire + arc additive manufacturing, Int. J. Fatigue 151 (2021), 106382.
[40] C. Xie, S. Wu, Y. Yu, H. Zhang, Y. Hu, M. Zhang, G. Wang, Defect-correlated fatigue resistance of additively manufactured Al-Mg4.5Mn alloy with in situ micro-rolling, J. Mater. Process Technol. 291 (2021), 117039.
[41] L. Bercelli, S. Moyne, M. Dhondt, C. Doudard, S. Calloch, J. Beaudet, A probabilistic approach for high cycle fatigue of Wire and Arc Additive Manufactured parts taking into account process-induced pores, Addit. Manuf. 42 (2021), 101989.
[42] C. Xue, Y. Zhang, P. Mao, C. Liu, Y. Guo, F. Qian, et al., Improving mechanical properties of wire arc additively manufactured AA2196 Al–Li alloy by controlling solidification defects, Addit. Manuf. 43 (2021), 102019.
[43] H. Bartsch, R. Kühne, S. Citarelli, S. Schaffrath, M. Feldmann, Fatigue analysis of wire arc additive manufactured (3D printed) components with unmilled surface, Structures 31 (2021) 576–589.
[44] P. Dirisu, G. Supriyo, F. Martina, X. Xu, S. Williams, Wire plus arc additive manufactured functional steel surfaces enhanced by rolling, Int. J. Fatigue 130 (2020), 105237.
[45] A. Ermakova, A. Mehmanparast, S. Ganguly, J. Razavi, F. Berto, Fatigue crack growth behaviour of wire and arc additively manufactured ER70S-6 low carbon steel components, Int. J. Fract. 235 (2022) 45–47.
[46] A. Ermakova, S. Ganguly, J. Razavi, F. Berto, A. Mehmanparast, Experimental investigation of the fatigue crack growth behavior in wire arc additively manufactured ER100S-1 steel specimens, Fatigue Fract. Eng. Mater. Struct. 45 (2022) 371–385.
[47] C. Huang, Y. Zheng, T. Chen, E. Ghafoori, L. Gardner, Fatigue crack growth behaviour of wire arc additively manufactured steels, Int. J. Fatigue 173 (2023), 107705.
[48] S. Mu, Y. Li, D. Song, B. Xu, X. Chen, Low cycle fatigue behavior and failure mechanism of wire arc additive manufacturing 16MND5 bainitic steel, J. Mater. Eng. Perform. 30 (2021) 4911–4924.
[49] About MX3D. Available from: https://mx3d.com/company/about/ [Accessed 25 June 2021].
[50] C. Li, H. Gu, W. Wang, S. Wang, L. Ren, Z. Wang, Z. Ming, Y. Zhai, Effect of heat input on formability, microstructure, and properties of Al–7Si–0.6 Mg alloys deposited by CMT-WAAM process, Appl. Sci. 10 (2019) 70.
[51] BSI (British Standards Institution) Aerospace series—metallic materials—test methods—constant amplitude fatigue testing. BS EN 6072:2010, Brussels, 2010.
[52] CEN (European Committee for Standardization) Metallic materials—tensile testing—Part 1: method of test at room temperature. EN ISO 6892-1:2016, Brussels, 2016.
[53] Standard practice for conducting force controlled constant amplitude axial fatigue tests of metallic materials. ASTM E466-21 2021 West Conshohocken, PA.
[54] Geomagic Wrap 2017–3D Systems (Version 2017.0.2:64) [Software] Incorporated and its Licensors, 2017.
[55] Rhino 3D (Version 7) [Software] Robert McNeel & Associates, 2020.
[56] Standard guide for preparation of metallographic specimens. ASTM E3-11 2011 West Conshohocken, PA.
[57] E. Ghafoori, M. Motavalli, A. Nussbaumer, A. Herwig, G.S. Prinz, M. Fontana, Design criterion for fatigue strengthening of riveted beams in a 120-year-old railway metallic bridge using pre-stressed CFRP plates, Compos Part B Eng. 68 (2015) 1–13.
[58] E. Ghafoori, M. Motavalli, A. Nussbaumer, A. Herwig, G.S. Prinz, M. Fontana, Determination of minimum CFRP pre-stress levels for fatigue crack prevention in retrofitted metallic beams, Eng. Struct. 84 (2015) 29–41.
[59] Standard practice for presentation of constant amplitude fatigue test results for metallic materials 2018 ASTM E468-18 West Conshohocken, PA.
[60] ABAQUS (Version 6.13–1) [Software] Hibbitt and Karlsson and Sorense, Pawtucket, RI, 2013.
[61] ISO (International Organization for Standardization) Industrial automation systems and integration—Product data representation and exchange—Part 21: Implementation methods: Clear text encoding of the exchange structure. ISO 10303–21:2016, London, 2016.
[62] S. Shojai, P. Schaumann, M. Braun, S. Ehlers, Influence of pitting corrosion on the fatigue strength of offshore steel structures based on 3D surface scans, Int. J. Fatigue 164 (2022), 107128.
[63] Pilkey W.D., Pilkey D.F., Bi Z. Peterson's stress concentration factors. 4th ed. John Wiley & Sons, 2020.
[64] Socie D., Marquis G. Multiaxial fatigue. SAE International, 1999.
[65] A. Fatemi, R. Molaei, S. Sharifimehr, N. Shamsaei, N. Phan, Torsional fatigue behavior of wrought and additive manufactured Ti-6Al-4V by powder bed fusion including surface finish effect, Int. J. Fatigue 99 (2017) 187–201.
[66] A. Fatemi, R. Molaei, S. Sharifimehr, N. Phan, N. Shamsaei, Multiaxial fatigue behavior of wrought and additive manufactured Ti-6Al-4V including surface finish effect, Int. J. Fatigue 100 (2017) 347–366.
[67] H.J. Gough, H.V. Pollard, The strength of metals under combined alternating stresses, Proc. Inst. Mech. Eng. 131 (1935) 3–103.
[68] Budynas, R.G., Nisbett J.K. Shigley's mechanical engineering design. 9th ed. McGraw-Hill, 2011.
[69] Neuber H. Theory of notch stresses: Principles for exact stress calculation. JW Edwards, 1946.
[70] O.H. Basquin, The exponential law of endurance tests, Proc. Am. Soc. Test. Mater. 10 (1910) 625–630.
[71] L. Susmel, R. Tovo, On the use of nominal stresses to predict the fatigue strength of welded joints under biaxial cyclic loading, Fatigue Fract. Eng. Mater. Struct. 27 (2004) 1005–1024.
[72] W. Wu, H. Kolstein, M. Veljkovic, Fatigue resistance of rib-to-deck welded joint in OSDs, analyzed by fracture mechanics, J. Constr. Steel Res. 162 (2019), 105700.
[73] C. Huang, T. Chen, Z. Xia, L. Jiang, Numerical study of surface fatigue crack growth in steel plates repaired with CFRP, Eng. Struct. 268 (2022), 114743.
[74] CEN (European Committee for Standardization) Eurocode 3—Design of Steel Structures—Part 1-9: Fatigue. EN 1993-1-9:2005, Brussels, 2005.
[75] A. Hobbacher, Recommendations for fatigue design of welded joints and components (IIW Collection), Institute of Cham: Springer International Publishing, 2016.
[76] A. Ermakova, J. Razavi, F. Berto, A. Mehmanparast, Uniaxial and multiaxial fatigue behaviour of wire arc additively manufactured ER70S-6 low carbon steel components, Int. J. Fatigue 166 (2023), 107283.
[77] M. Braun, L. Kellner, Comparison of machine learning and stress concentration factors-based fatigue failure prediction in small-scale butt-welded joints, Fatigue Fract. Eng. Mater. Struct. (2022) 3403–3417.
[78] V. Okorokov, D. MacKenzie, Y. Gorash, M. Morgantini, R. van Rijswick, T. Comlekci, High cycle fatigue analysis in the presence of autofrettage compressive residual stress, Fatigue Fract. Eng. Mater. Struct. 41 (2018) 2305–2320.
[79] M. Morgantini, D. Mackenzie, T. Comlekci, R. van Rijswick, The effect of mean stress on corrosion fatigue life, Procedia Eng. 213 (2018) 581–588.
[80] Ulewicz R., Szataniak P., Novy F. Fatigue properties of wear resistant martensitic steel. In 23rd International conference on metallurgy and materials, 2014:784–9.
[81] S. Anandavijayan, A. Mehmanparast, J. Braithwaite, F. Brennan, A. Chahardehi, Material pre-straining effects on fatigue behaviour of S355 structural steel, J. Constr. Steel Res 183 (2021), 106707.
[82] R. Dantas, J. Correia, G. Lesiuk, D. Rozumek, S.P. Zhu, A. de Jesus, L. Susmel, F. Berto, Evaluation of multiaxial high-cycle fatigue criteria under proportional loading for S355 steel, Eng. Fail Anal. 120 (2021), 105037.
[83] P. Corigliano, F. Cucinotta, E. Guglielmino, G. Risitano, D. Santonocito, Fatigue assessment of a marine structural steel and comparison with Thermographic Method and Static Thermographic Method, Fatigue Fract. Eng. Mater. Struct. 43 (2020) 734–743.